Article

Neuron

Nanoscale Mobility of the Apo State and TARP Stoichiometry Dictate the Gating Behavior of Alternatively Spliced AMPA Receptors

Graphical Abstract

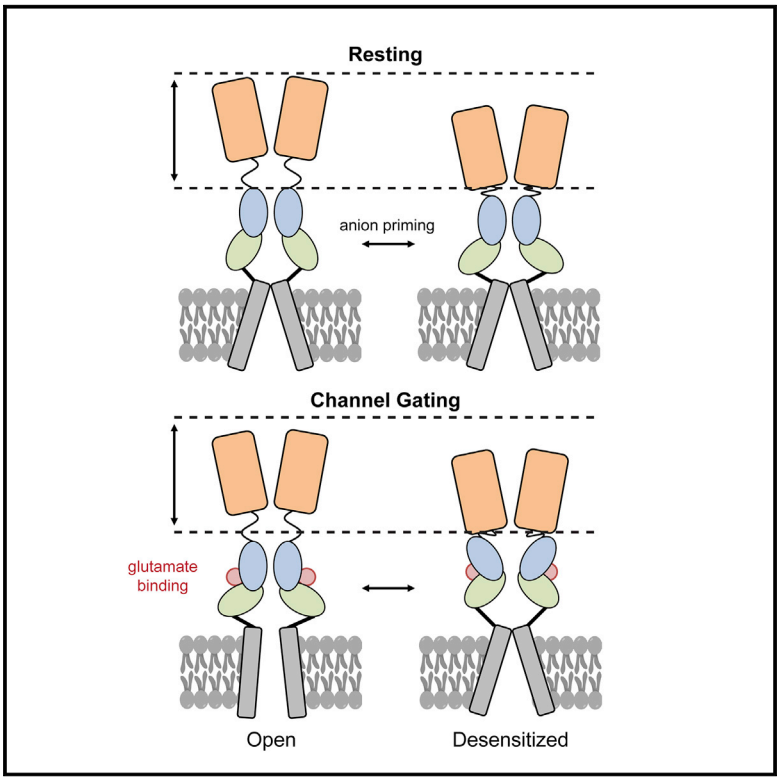

Authors

G. Brent Dawe, Md. Fahim Kadir, Raminta Venskutonytė, ..., Jette S. Kastrup, J. Michael Edwardson, Derek Bowie

Correspondence

derek.bowie@mcgill.ca

In Brief

Combining electrophysiology, atomic force microscopy, and X-ray crystallography, Dawe et al. reveal that nanoscale mobility of the apo state and TARP stoichiometry coordinate the responsiveness of alternatively spliced AMPA receptors to neurotransmitter, allosteric anions, and TARP auxiliary proteins.

Highlights

- Nanoscale mobility of the apo state predetermines gating of flip/flop AMPA receptors
- The flip/flop cassette exerts long-range control on the distant N-terminal domain
- TARP stoichiometry further dictates the functionality of flip/flop AMPA heteromers
- Neurons express two AMPA receptor classes that are either partially or fully TARPed

Dawe et al., 2019, Neuron *102*, 1–17
June 5, 2019
https://doi.org/10.1016/j.neuron.2019.03.046

CellPress

Please cite this article in press as: Dawe et al., Nanoscale Mobility of the Apo State and TARP Stoichiometry Dictate the Gating Behavior of Alternatively Spliced AMPA Receptors, Neuron (2019), https://doi.org/10.1016/j.neuron.2019.03.046

Neuron
Article

Nanoscale Mobility of the Apo State and TARP Stoichiometry Dictate the Gating Behavior of Alternatively Spliced AMPA Receptors

G. Brent Dawe,[1,2,6] Md. Fahim Kadir,[3,6] Raminta Venskutonytė,[4,6] Amanda M. Perozzo,[1,2] Yuhao Yan,[1,2] Ryan P.D. Alexander,[1,2] Camilo Navarrete,[3,5] Eduardo A. Santander,[3] Marika Arsenault,[2] Christian Fuentes,[3,5] Mark R.P. Aurousseau,[2] Karla Frydenvang,[4] Nelson P. Barrera,[5] Jette S. Kastrup,[4,7] J. Michael Edwardson,[3,7] and Derek Bowie[2,7,8,*]

[1]Integrated Program in Neuroscience, McGill University, Montréal, QC H3A 2B4, Canada
[2]Department of Pharmacology and Therapeutics, McGill University, Montréal, QC H3G 1Y6, Canada
[3]Department of Pharmacology, University of Cambridge, Cambridge CB2 1PD, UK
[4]Department of Drug Design and Pharmacology, University of Copenhagen, 2100 Copenhagen, Denmark
[5]Department of Physiology, Pontificia Universidad Católica de Chile, 8331150 Santiago, Chile
[6]These authors contributed equally
[7]Senior Author
[8]Lead Contact
*Correspondence: derek.bowie@mcgill.ca
https://doi.org/10.1016/j.neuron.2019.03.046

SUMMARY

Neurotransmitter-gated ion channels are allosteric proteins that switch on and off in response to agonist binding. Most studies have focused on the agonist-bound, activated channel while assigning a lesser role to the apo or resting state. Here, we show that nanoscale mobility of resting α-amino-3-hydroxy-5-methyl-4-isoxazolepropionic acid (AMPA)-type ionotropic glutamate receptors (AMPA receptors) predetermines responsiveness to neurotransmitter, allosteric anions and TARP auxiliary subunits. Mobility at rest is regulated by alternative splicing of the flip/flop cassette of the ligand-binding domain, which controls motions in the distant AMPA receptor N-terminal domain (NTD). Flip variants promote moderate NTD movement, which establishes slower channel desensitization and robust regulation by anions and auxiliary subunits. In contrast, greater NTD mobility imparted by the flop cassette acts as a master switch to override allosteric regulation. In AMPA receptor heteromers, TARP stoichiometry further modifies these actions of the flip/flop cassette generating two functionally distinct classes of partially and fully TARPed receptors typical of cerebellar stellate and Purkinje cells.

INTRODUCTION

α-Amino-3-hydroxy-5-methyl-4-isoxazolepropionic acid (AMPA)-type ionotropic glutamate receptors (iGluRs) mediate most fast-excitatory neurotransmission in the mammalian brain (Dingledine et al., 1999; Traynelis et al., 2010). They form the hardwiring of glutamatergic circuits but also strengthen or weaken synaptic transmission during periods of sustained patterned activity or altered homeostasis (Herring and Nicoll, 2016; Turrigiano, 2017). AMPA receptors are also implicated in numerous CNS disorders and thus are targeted for the development of clinically relevant compounds (Bowie, 2008). Consequently, there has been a concerted effort to provide a full understanding of the structural and functional aspects of AMPA receptor signaling.

AMPA receptors assemble as tetramers in either a homomeric (Sobolevsky et al., 2009) or heteromeric (Herguedas et al., 2016, 2019) subunit arrangement that may additionally include accessory subunits such as the transmembrane AMPA receptor regulatory proteins (TARPs) and cornichon families (Greger et al., 2017; Jackson and Nicoll, 2011) (Figure 1A). The AMPA receptor subunit is composed of four functional domains that include (1) a cytoplasmic C-terminal domain (CTD; not shown in Figure 1A) that directs receptor trafficking and synaptic anchoring (Shepherd and Huganir, 2007); (2) a transmembrane domain (TMD), which forms a central ion channel pore that rapidly transports Na^+ and Ca^{2+} ions in response to binding of the neurotransmitter, L-glutamate (L-Glu) (Dingledine et al., 1999; Traynelis et al., 2010); (3) a clamshell-like ligand-binding domain (LBD; Figure 1B) (Mayer and Armstrong, 2004); and (4) an N-terminal domain (NTD), which directs subunit assembly and receptor clustering at synapses (García-Nafría et al., 2016).

In addition to these four distinct regions of the overall tetrameric structure, the LBD dimer interface has been shown to be critical in determining the time course of AMPA receptor gating (Dawe et al., 2015). Specifically, recent work from our lab has identified a novel cation-binding pocket that promotes channel activation by the formation of a network of electrostatic interactions at the apex of both the AMPA receptor (Dawe et al., 2016) and the kainate receptor (Dawe et al., 2013) LBD dimer interfaces. Interestingly, anions have also been shown to control

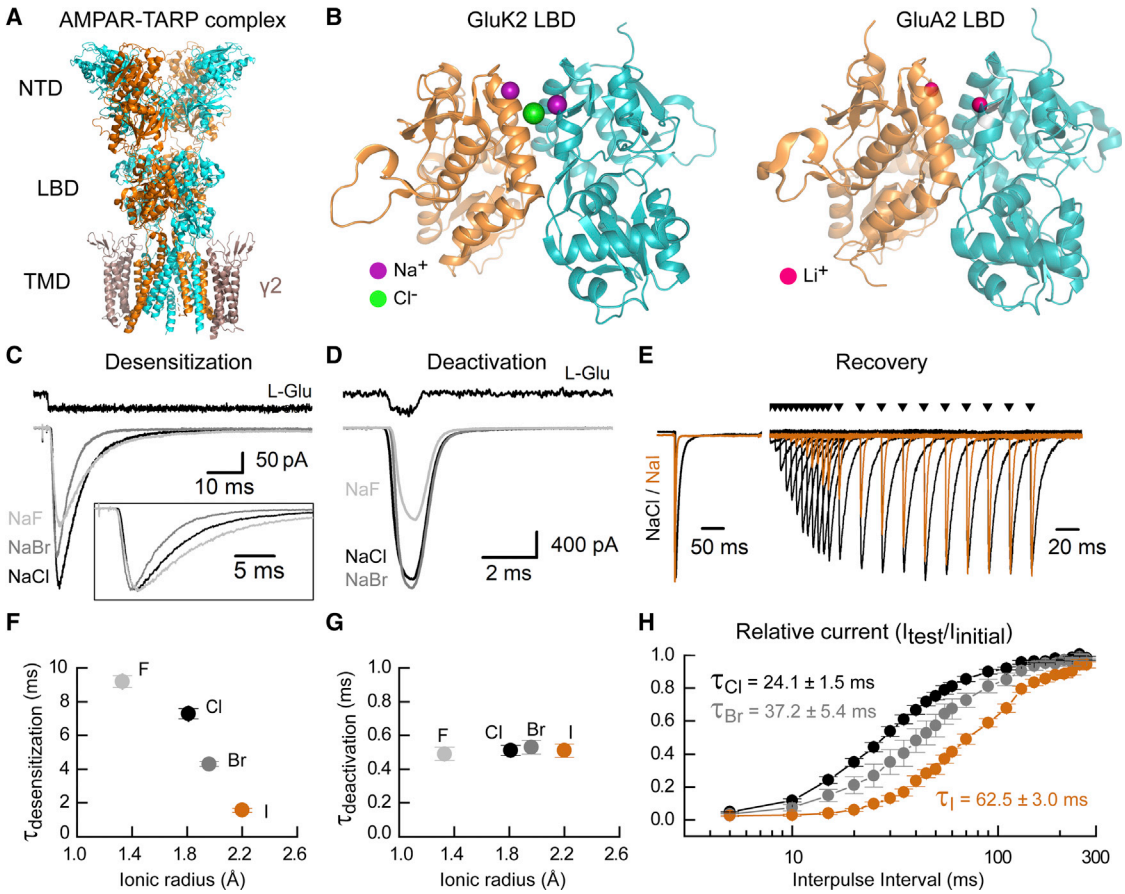

Figure 1. External Anions Selectively Modulate AMPA Receptor Desensitization

(A) Cryo-EM structure of the GluA2-TARP γ2 (pale pink) receptor complex (PDB: 5KBU) in an antagonist-bound form.

(B) Side view of the GluK2 (left, PDB: 3G3F) and GluA2 (right, PDB: 4IGT) LBD dimer, depicting the binding pockets for two Na^+ ions (purple) and one Cl^- ion (green) in GluK2 and two Li^+ ions (magenta) in GluA2.

(C and D) Typical current responses of $GluA2_i$ receptors to a 250 ms (C; patch 140228p6) or 1 ms (D; patch 150825p10) application of 10 mM L-Glu in external NaCl (black), NaBr (gray), and NaF (light gray). Inset: responses scaled to compare decay kinetics. The uppermost trace (black) shows the junction current recorded after the experiment to monitor the solution exchange rate.

(E) Recovery from desensitization for $GluA2_i$ receptors (patch 151201p9) in external NaCl (black) and NaI (orange).

(F and G) Mean time constants of current decay after 250 ms (F; $\tau_{desensitization}$) or 1 ms (G; $\tau_{deactivation}$) L-Glu applications plotted against ionic radius. Data represent mean ± SEM from 7 to 15 (F) or 5 to 12 (G) independent patch experiments.

(H) Recovery from desensitization experiments in different external anion solutions. Data represent mean ± SEM from 6 (NaI), 7 (NaBr), or 13 (NaCl) independent patch experiments. See also Table S1.

the time course of AMPA receptor gating (Bowie, 2002); however, the structural basis of this mechanism has yet to be understood. Another unresolved issue related to AMPA receptor gating is the possible role of the NTD in channel gating. Recent work has highlighted the dynamic motions in the NTD of both AMPA- and kainate-type iGluRs (Dürr et al., 2014; Dutta et al., 2015; Matsuda et al., 2016; Meyerson et al., 2014; Nakagawa et al., 2005) and interactions with auxiliary proteins (Cais et al., 2014; Möykkynen et al., 2014; Shaikh et al., 2016) that may facilitate transsynaptic contact formation (García-Nafría et al., 2016) and permit AMPA receptor trafficking during synapse strengthening (Díaz-Alonso et al., 2017; Watson et al., 2017). Since structural rearrangements of the NTD accompany receptor desensitization (Dürr et al., 2014; Meyerson et al., 2014; Nakagawa et al., 2005; Twomey et al., 2017a), it has been assumed that the underlying movement is triggered by agonist binding. However, it is also possible that the intrinsic thermodynamic mobility of the resting AMPA receptor determines NTD movement and its responsiveness to agonist.

Here, we have designed experiments to distinguish between these two possibilities. Our data identify a novel allosteric anion-binding pocket at the alternatively spliced flip/flop cassette that modifies NTD motions in the resting state prior to agonist binding and regulates channel gating in the presence and absence of auxiliary subunits. Ser775 of the GluA2flip isoform ($GluA2_i$) renders AMPA receptors sensitive to anion modulation, whereas Asn775 of the GluA2flop isoform ($GluA2_o$) almost eliminates the effects of anions on the NTD and channel

gating. Imaging by atomic force microscopy (AFM) reveals that the NTDs of GluA2$_o$ receptors are more mobile than those of GluA2$_i$ receptors, indicating differences in the intrinsic conformational flexibility of their resting states. This behavior is interchangeable via a single amino acid, the Ser775 residue, that operates as a molecular switch between flip and flop isoforms. TARP stoichiometry further modifies these actions of the flip/flop cassette on AMPA receptor heteromers, generating two distinct classes of partially and fully TARPed GluA1/A2 receptors that match the functional profile of native AMPA receptors expressed by cerebellar stellate and Purkinje cells, respectively.

RESULTS

Anions Modulate AMPA Receptor Desensitization

Although the structural and functional bases of anion and cation modulation of kainate receptors have been studied extensively (Bowie, 2002, 2010; Dawe et al., 2013; Wong et al., 2006), much less is known about the effect of external ions on AMPA receptors. Recent work identified the structural mechanism of cation regulation (Figure 1B) (Dawe et al., 2016); however, the nature of anion modulation of AMPA receptors (Bowie, 2002) remains unknown. The effect of external anions on AMPA receptor deactivation and desensitization was studied by recording agonist-evoked membrane currents in outside-out membrane patches excised from HEK293 cells expressing GluA2$_i$(Q) (Figures 1C–1H; see STAR Methods). As observed previously for GluA1$_i$ receptors (Bowie, 2002), the time course of entry into desensitization for GluA2$_i$ was sensitive to external halides, accelerating 1.7- and 4.6-fold in bromide (τ = 4.3 ± 0.2 ms; n = 7) and iodide (τ = 1.6 ± 0.1 ms; n = 7), respectively, compared to chloride (τ = 7.3 ± 0.3 ms; n = 15) (Figures 1C and 1F; Table S1). In contrast, deactivation rates were almost identical for all anions tested on GluA2$_i$ (Figures 1D and 1G; Table S1). In keeping with this, recovery rates out of desensitization were also anion dependent, with GluA2$_i$ recovering from desensitization ~3-fold more slowly in external iodide ($\tau_{recovery}$ = 62.5 ± 3.0 ms; n = 6) than in external chloride ($\tau_{recovery}$ = 24.1 ± 1.5 ms; n = 13) (Figures 1E and 1H; Table S1). Interestingly, rates into and out of desensitization have a predictive relationship with the ionic radius of the external anion (Figures 1F and 1H), with faster desensitization rates observed with anions of a larger radius. The relationship between ionic radius and channel desensitization is consistent with the existence of a specific anion-binding pocket. Previous work has located cation-binding pockets critical to AMPA and kainate receptor gating to the interface of LBD dimers (Dawe et al., 2013, 2016) (Figure 1B); consequently, we reasoned that anions might bind to this region too. Moreover, previous work has demonstrated the important role of the LBD dimer interface in regulating AMPA receptor gating, including desensitization (Dawe et al., 2015; Horning and Mayer, 2004; Sun et al., 2002).

To determine the location of the anion-binding pocket, two soluble constructs of the GluA2-LBD were crystallized in the presence of bromide ions (Figure 2). Since bromide ions give anomalous scattering, we used this property to identify the position of the bound bromide ions in the structure and to distinguish them from other ions and water molecules in the X-ray diffraction data (Figures 2A–2D), as also previously done for localization of the anion-binding site in kainate receptors (Plested and Mayer, 2007). Two X-ray structures were determined that correspond to the flop isoform (GluA2$_o$-LBD; PDB: 6GL4) and the flip-like mutant GluA2$_o$-LBD N775S (PDB: 6GIV). The structures are shown in Figures 2 and S1 along with statistics of data collection and refinement in Table S2. The anomalous scattering data clearly indicate the location of two bromide ions near the base of the D1-D1 dimer interface in both structures (Figures 2C, 2D, and S1A–S1C). More specifically, these anion-binding sites are in a hydrophobic space, surrounded by Pro515 and Leu772 from one subunit, Ile502, Leu504, and Pro515 from the partner subunit, and capped by Lys514 (Figures 2E, 2F, S1D, S1E, S2A, and S2B). There are also several water molecules surrounding each bromide, separating the ion from Ser775 (Figures 2C–2F). Interestingly, we also determined a structure of GluA2$_o$-LBD in the presence of a high concentration of chloride ions, and the electron density indicated that chloride ions bind to the same location as bromide in the LBD dimer interface (data not shown).

Ser775 is notable for interacting with positive modulators of AMPA receptors (Figure S1F) such as cyclothiazide (CTZ) (Partin et al., 1996), as well as being one of the residues that forms the alternatively spliced flip/flop cassette (Sommer et al., 1990). Given the high affinity for CTZ, we hypothesized that it would displace bromide ions from their bound positions. In agreement with this, electrophysiological responses observed in different external anions were non-decaying in each case (Figures S1G and S1H), consistent with the idea that CTZ outcompetes external anions for binding. Likewise, mutation of Leu504 to an Ala or Cys residue either reversed or eliminated anion regulation of GluA2$_i$ receptor decay kinetics, respectively (Figures S2C–S2F), further validating the location of the anion-binding pocket as being at the LBD dimer interface. Taken together, these results identify an anion-binding pocket, which, when occupied by halide ions, may be responsible for regulating the rates of entry into and exit from AMPA receptor desensitization.

The Ser/Asn Residue Regulates Anion Effects

To establish a causal relationship between the anion-binding pocket and the functional effects of external anions on GluA2, we focused on position 775, which, as mentioned previously, is modified by alternative splicing and is also involved in all regulatory effects of the flip/flop cassette (see below). The flip isoform of the AMPA receptor contains a Ser at position 775 whereas the flop isoform contains an Asn (Figures 3A and 3B) (Sommer et al., 1990), which we hypothesized may differentially affect anion modulation of AMPA receptors.

To test this, we first compared the effect of external anions on desensitization rates of GluA2$_i$ and GluA2$_o$ receptors, whose amino acid sequences differ at nine residues (Figure 3A) (Sommer et al., 1990). As anticipated, GluA2$_i$ and GluA2$_o$ receptors differed in their sensitivity to modulation by external ions (Figures 3C and 3D), though the trend of faster desensitization in the presence of larger anions persisted (Figure 3F). For example, in GluA2$_o$ receptors, iodide accelerated rates into desensitization

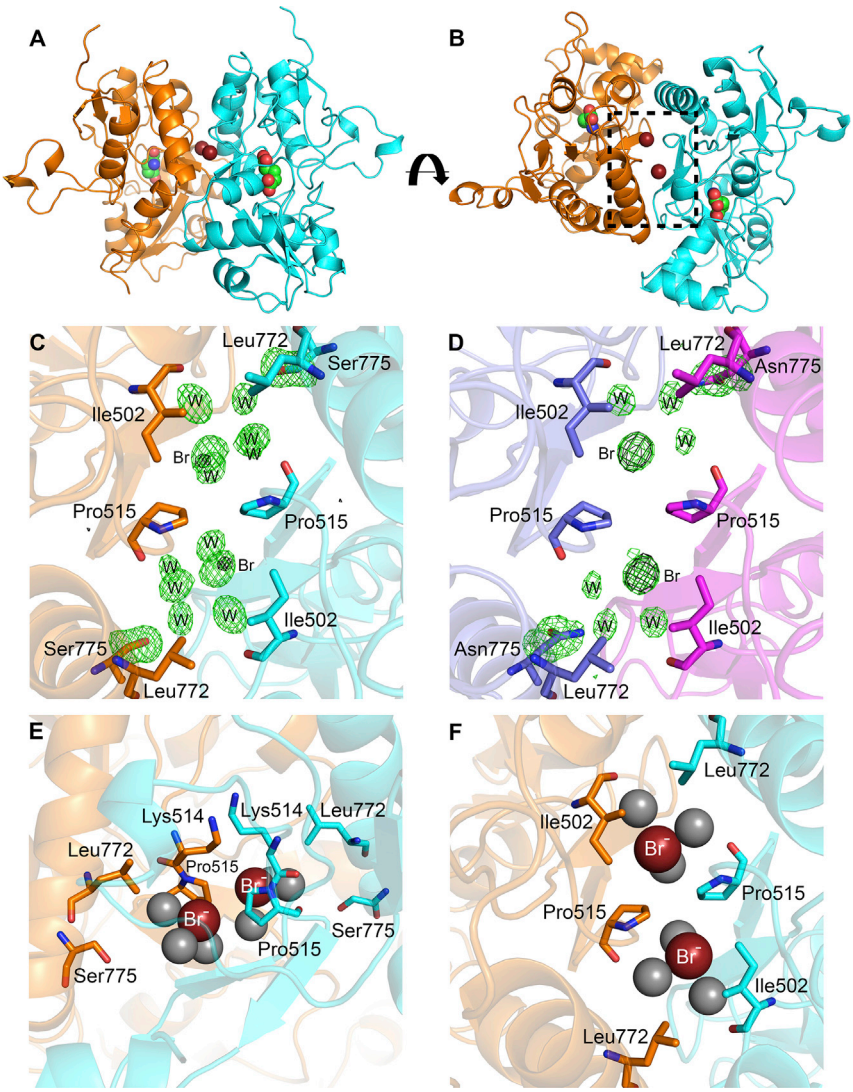

Figure 2. Detection of Bromide Ions in the GluA2-LBD Dimer Interface

(A and B) Side (A) and top (B) views of the GluA2$_o$-LBD N775S dimer. Bromide ions are shown in the dimer interface as brown spheres and glutamate with carbon atoms as green spheres. Nitrogen atoms are blue, and oxygen atoms are red.

(C and D) Anomalous difference electron density map (black; contoured at 7σ, before introduction of bromide ions in the structure) and Fo-Fc difference map (green; contoured at 3σ) from omitting Ser775/Asn775, bromide ions, and water molecules within 4 Å of bromide from GluA2$_o$-LBD N775S (C) and GluA2$_o$-LBD (chain A) (D).

(E and F) Magnified side (E) and top (F) views of the bromide-binding sites in the GluA2$_o$-LBD N775S dimer interface. Water molecules are shown as gray spheres, and amino acid residues surrounding the binding sites are shown as orange or cyan sticks based on their subunit of origin.

See also Figure S1 and Table S2.

~1.6-fold (τ = 0.8 ± 0.05 ms; n = 6) compared to chloride (τ = 1.3 ± 0.06 ms; n = 12), which was substantially less than the 4.6-fold difference observed on GluA2$_i$ receptors (Figures 3C, 3D, and 3F; Table S1). To examine whether this difference was due to residue 775, which is in close proximity to the bromide-binding site (Figure 2E), we repeated these experiments on the Ser775Asn GluA2$_i$ receptor (Figures 3E and 3F; Table S1). As anticipated, the GluA2$_i$ S775N receptor was much less sensitive to modulation by external anions. For example, iodide (τ = 3.6 ± 0.5 ms; n = 6) accelerated desensitization compared to chloride (τ = 5.2 ± 0.4 ms; n = 12) by only 1.4-fold (Figures 3E and 3F; Table S1). In contrast, mutation of the two more apical dimer interface residues that contribute to fast GluA2$_o$ desensitization (Figure 3B) (Quirk et al., 2004) produced a receptor (T765N/P766A) that still exhibited robust anion sensitivity (Figure S3). As a result, the near loss of anion modulation from flip- to flop-type GluA2 AMPA receptors can be primarily attributed to Asn775, consistent with our structural data placing bromide ions in the lower D1-D1 LBD dimer interface. Interestingly, anion modulation of recovery from desensitization was still present in GluA2$_i$ S775N receptors (Figures 3G and 3H), demonstrating that anion effects on rates into and out of desensitization have different mechanisms.

Anions Control Resting and Active AMPA Receptors

Anions may affect AMPA receptors by controlling the receptor's resting and/or activated state(s). To delineate between these possibilities, we investigated whether external halides elicited global, conformational changes in protein structure in the absence and/or presence of agonist. Specifically, we measured protein height as an indicator of conformation using AFM, since AMPA receptor activation and desensitization involve compression in the quaternary structure (Dürr et al., 2014; Herguedas et al., 2016; Meyerson et al., 2014; Twomey et al., 2017a, 2017b) as in NMDA-type iGluRs (Balasuriya et al., 2014; Suzuki et al., 2013). To image the receptor, we purified and reconstituted individual AMPA receptor complexes into lipid bilayers (Figures 4 and S4; see STAR Methods).

The addition of L-Glu to NaCl-based external solution prompted a 0.69 ± 0.11 nm (n = 11) reversible reduction in GluA2$_i$ receptor height (Figures 4A, 4C, and S5), which was prevented by the competitive antagonist, 6-cyano-7-nitroquinoxaline-2,3-dione (CNQX), and the positive allosteric modulator, CTZ (Table S3; Figure S5). AFM experiments were also repeated to determine if height changes could be induced by different anions (Figures 4B, 4D, and S5; Table S3). Unexpectedly, merely changing the main external anion species from NaCl to NaBr (0.74 ± 0.06 nm; n = 12) or NaI (0.87 ± 0.11 nm; n = 13) produced a substantial and reversible vertical compression of individual GluA2$_i$ receptors (Figures 4D and S5) comparable to L-Glu-evoked

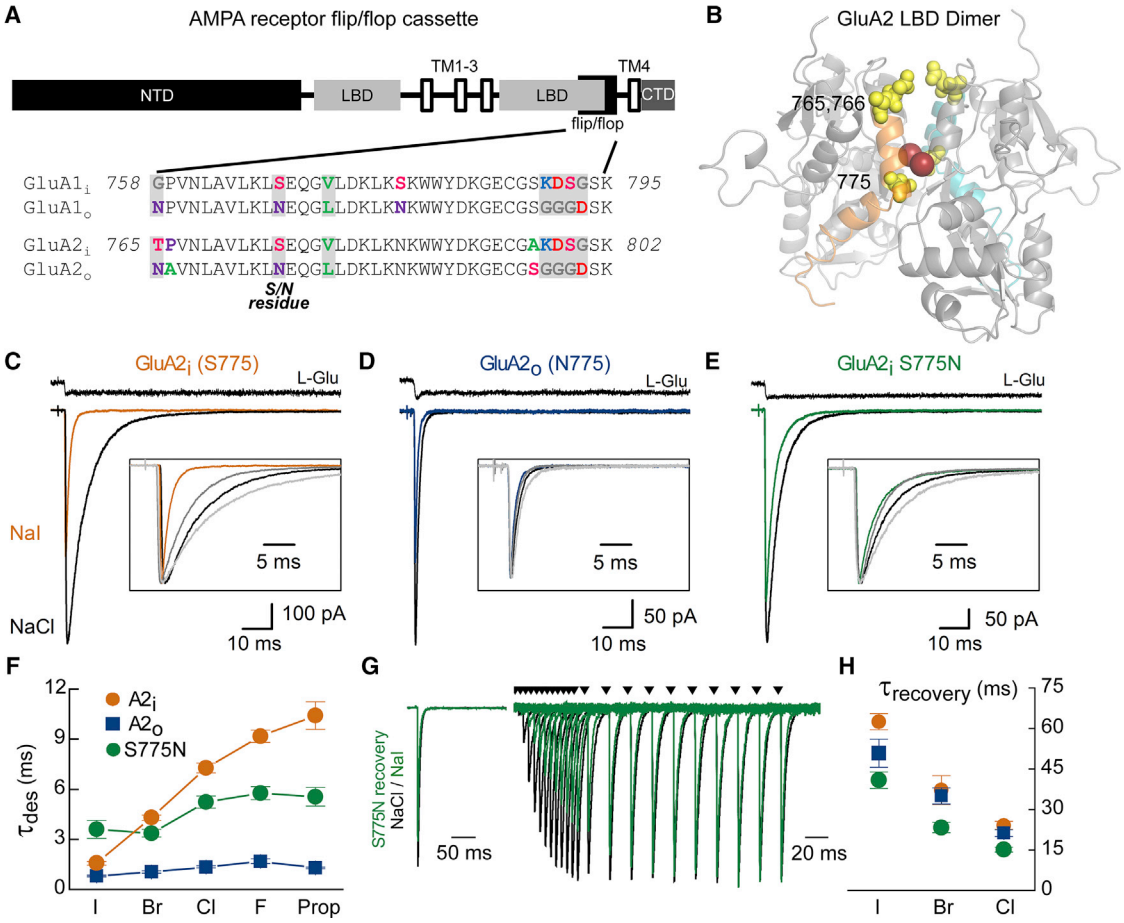

Figure 3. The Ser/Asn 775 Residue of the Flip/Flop Cassette Governs Anion Modulation of AMPA Receptors

(A) Sequence alignment of the GluA1 and GluA2 AMPA receptor flip/flop cassette, located toward the C-terminal end of the LBD. Positions that differ in both subunits are shaded gray, while residues are colored by chemical property (blue, positive charge; red, negative charge; pink, small polar; purple, large polar; green, hydrophobic).

(B) GluA2$_o$-LBD dimer with residues Asn765, Ala766, and Asn775 shown as yellow spheres and the two bromide ions as brown spheres. The flip/flop cassette is orange in one subunit and cyan in the other subunit.

(C–E) Typical current responses (250 ms, 10 mM L-Glu) of GluA2$_i$ (C; patch 151123p15), GluA2$_o$ (D; patch 160218p14), and GluA2$_i$ S775N (E; patch 160119p3) receptors in external NaCl (black) and NaI (colored trace). Inset: scaled responses in external NaI (colored trace), NaBr (gray), NaCl (black), and NaF (light gray). The uppermost trace (black) shows the junction current recorded after the experiment to monitor solution exchange rate.

(F) Desensitization time constants for data shown in (C)–(E), plotted against different halide ions. Data represent mean ± SEM from 6 to 15 independent patch experiments. Prop refers to propionate.

(G) Recovery from desensitization of GluA2$_i$ S775N receptors (patch 160401p15) in external NaCl (black) and NaI (green).

(H) Mean time constants of recovery from desensitization for GluA2$_i$ (orange), GluA2$_o$ (blue), and GluA2$_i$ S775N (green) in different external anions. Data represent mean ± SEM from 5 to 32 independent patch experiments.

See also Figures S2 and S3 and Table S1.

responses (Figure 4C). Interestingly, much less additional compression (~0.2 nm) was observed when L-Glu (10 mM) was added to NaBr or NaI solutions (Figure 4C), suggesting the principal role of anions is to prime the receptor. Since the action of L-Glu, however, was not entirely occluded, the structural rearrangements observed with anion substitution must differ from those elicited by agonist binding.

To establish a relationship between anion-induced height changes (Figure 4D) and their effect on desensitization (Figures 1C and 1F), we repeated AFM measurements on GluA2$_o$, whose gating properties are relatively anion insensitive. Remarkably, anion-induced height compression was almost completely absent from the GluA2$_o$ receptor when external solution containing NaCl was switched to either NaBr (0.03 ± 0.06 nm; n = 14) or NaI (0.08 ± 0.06 nm; n = 14) (Figure 4D; Table S3). Importantly, agonist binding continued to elicit reductions in the height of all anion species (Figure 4C), reaffirming that anion and agonist effects are different. In agreement with our electrophysiology data, iodide anions did not affect the AFM-reported height changes of GluA2$_i$ receptors containing the single S775N point mutation (Figure 4D; Table S3), establishing a critical role for the Ser/Asn residue and causal relationship between the effects

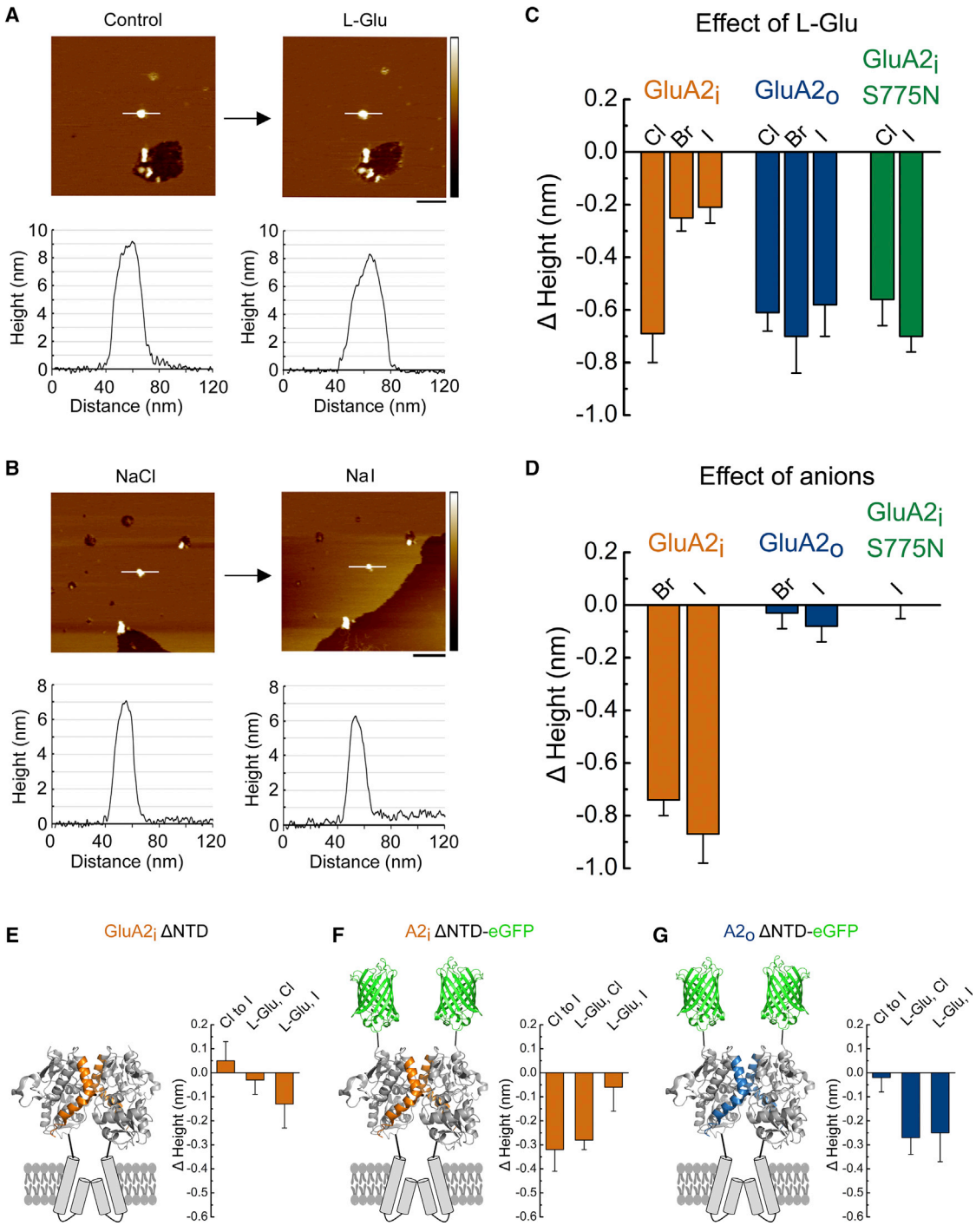

Figure 4. Anions Control the Resting and Active Quaternary Structure of the AMPA Receptor through the LBD

(A) Top: representative AFM images of a bilayer containing $GluA2_i$ receptors before (left) and after (right) application of L-Glu (10 mM). Scale bar, 100 nm; color-height scale, 0–10 nm. Bottom: sections through the receptor at the position indicated by the white line above.

(B) Top: representative AFM images of a bilayer containing $GluA2_i$ receptors before (left) and after (right) a switch from NaCl to NaI. Scale bar, 100 nm; color-height scale, 0–10 nm. Bottom: sections through the receptor at the position indicated by the white line above.

(C) Average height changes of $GluA2_i$, $GluA2_o$, and $GluA2_i$ S775N in response to L-Glu. Data represent mean ± SEM for 10–14 receptors.

(D) Average height changes of $GluA2_i$, $GluA2_o$ and $GluA2_i$ S775N in response to anion switches. Data represent mean ± SEM for 12–14 receptors.

(legend continued on next page)

of anions on channel gating and height changes. Finally, AFM-reported height changes elicited by switches in external anions were absent from the GluA2$_i$ L504A receptor, whereas L-Glu persisted in reducing height in all anion species tested (Figures S2G and S2H; Table S3).

Taken together, these data indicate two important points. First, external anions prime the receptor prior to activation. Whether priming then determines the rate of AMPA receptor desensitization prior to agonist binding is investigated below. Second, anion modulation reveals a coupling between the LBD dimer interface and the NTD. This latter possibility was examined in additional AFM experiments on GluA2 lacking the NTD (i.e., GluA2 ΔNTD).

The Flip/Flop Cassette Controls NTD Motions

Anion- and agonist-induced height changes were repeated using the truncated GluA2$_i$ ΔNTD receptor (Figures 4E–4G and S6). Contrary to wild-type behavior, virtually no height changes could be induced in the GluA2$_i$ ΔNTD receptor by replacing NaCl with NaI (−0.05 ± 0.08 nm; n = 15) or by agonist application (in NaCl, 0.03 ± 0.06 nm; n = 13) (Figure 4E; Table S3), demonstrating that receptor compression requires the NTD. To explore this further, we reengineered GluA2$_i$ and GluA2$_o$ receptors, replacing each NTD with an EGFP molecule (Figures 4F and 4G). Importantly, the expressed GluA2 ΔNTD-EGFP constructs exhibited similar functional behavior in terms of anion sensitivity and responsiveness to agonist (data not shown). We reasoned that although anions and agonists bind to the LBD, the energy of binding might induce a conformational change that is more prominently observed in distant regions of the protein, even if the NTD is replaced by EGFP. Consistent with this, compression induced by external anions (NaCl to NaI, 0.32 ± 0.09 nm; n = 18) and agonist application (in NaCl 0.28 ± 0.04 nm; n = 10) was restored in the GluA2$_i$ ΔNTD-EGFP construct, demonstrating that binding events in the LBD are transferred to the NTD. Since the GluA2$_i$ ΔNTD-EGFP construct retained the original linker sequences, we reasoned that the linkers might exert a similar downward pulling force on whatever is attached above. Since EGFP has a different size and likely does not form intersubunit dimers, these distinctions may explain why height changes were ~2-fold less with GluA2$_i$ ΔNTD-EGFP. Finally, agonist, but not anion, binding induced compression of the GluA2$_o$ ΔNTD-EGFP construct (Figure 4G), confirming that compression of the NTD is differentially controlled by the flip/flop cassette. Given this, we next tested if the intrinsic motions in resting GluA2 AMPA receptors may be a critical factor in determining its anion and agonist responsiveness.

AMPA Receptors Have Different Resting States

AFM visualization of the NTD movements of the GluA2 AMPA receptor (Figure 5) revealed that both isoforms exist as two distinct globular structures, which show mobility even in the resting state (Figure 5A; Videos S1 and S2). Unexpectedly, NTD movements at rest, expressed as cumulative squared displacement (CSD), were almost 3-fold greater for GluA2$_o$ (resting CSD, 15.53 ± 2.54 nm^2, n = 7) than for GluA2$_i$ (resting CSD, 5.58 ± 0.92 nm^2, n = 5) (Figures 5B and 5D; Table S4), revealing that NTD motions are controlled by the flip/flop cassette. Bath application of a saturating concentration of L-Glu (10 mM) increased the NTD mobility of the GluA2$_i$ AMPA receptor (CSD, 13.90 ± 2.11 nm^2, n = 9), but not that of GluA2$_o$ (CSD, 17.12 ± 0.59 nm^2, n = 5) (Figures 5C and 5D; Videos S3 and S4). As expected, the NTD mobility in the presence of L-Glu was reduced by CNQX for both GluA2$_i$ (5.33 ± 0.82 nm^2, n = 4) and GluA2$_o$ (9.50 ± 1.95 nm^2, n = 3) (Figure 5D; Table S4) demonstrating a direct relationship between NTD mobility and agonist binding. NTD movement of GluA2$_i$ was agonist-concentration dependent (Figure 5E; Table S4), whereas the mobility of GluA2$_o$ was not. Most importantly, the NTD mobility of the GluA2$_i$ S775N mutant (resting CSD, 14.00 ± 1.70, n = 9) was also greater than that of wild-type GluA2$_i$, but not GluA2$_o$ (Figure 5B; Table S4). This observation is important, as it establishes a causal link between the effects of anions on channel gating (Figures 1 and 3) and height changes (Figure 4) with the resting state of the AMPA receptor.

Given this, we reasoned that the lower conformational mobility of the GluA2$_i$ receptor at rest would favor more stable interactions in regions of the protein, such as the LBD dimer interface (Dawe et al., 2015, 2016). A more stable AMPA receptor structure would also favor anion binding to the LBD dimer interface and account for the greater effect of external halide ions on GluA2$_i$ receptors. Conversely, the higher mobility of the GluA2$_o$ receptor would disfavor anion binding (and its regulation) and destabilize the open state of the receptor, explaining its much more rapid desensitization kinetics and weaker anion sensitivity. Given this, we concluded that the flop cassette of the AMPA receptor acts as a master switch that overrides allosteric mechanisms, such as anion regulation that impacts the time AMPA receptors remain in the open state. We therefore hypothesized that GluA2$_o$ should also be similarly insensitive to regulation by auxiliary proteins, such as the prototypical TARP, stargazin (γ2).

To test this hypothesis, we compared the electrophysiological responses of GluA2$_i$, GluA2$_o$, and GluA2$_i$ S775N receptors expressed with γ2 (Figures 6A–6D). As noted previously (Dawe et al., 2016), co-assembly of GluA2$_i$ receptors with γ2 slowed desensitization rates (τ_{des}, ms) and reduced equilibrium desensitization ($I_{equilibrium}$, %) by ~4-fold and 22-fold, respectively (Figures 6A, 6C, and 6D; Table S1). Desensitization rates and equilibrium desensitization were also anion sensitive, exhibiting a rank order of potency similar to that described for GluA2$_i$ receptors alone (Figures 6B–6D; Table S1). In contrast, co-assembly of GluA2$_o$ receptors with γ2 almost eliminated the effect of the TARP on desensitization rates, equilibrium desensitization, and anion regulation (Figures 6A–6D; Table S1), in agreement with

(E–G) Mean height changes of GluA2$_i$ ΔNTD (E), A2$_i$ ΔNTD-EGFP (F), and A2$_o$ ΔNTD-EGFP (G) receptors in response to anion substitution as well as 10 mM L-Glu application in different external anions. Data represent mean ± SEM for 10–22 receptors. Cartoon uses GFP (PDB: 1GFL) and AMPA receptor LBD (PDB: 1FTJ) structures for illustrative purpose only.
See also Figures S4–S6 and Table S3.

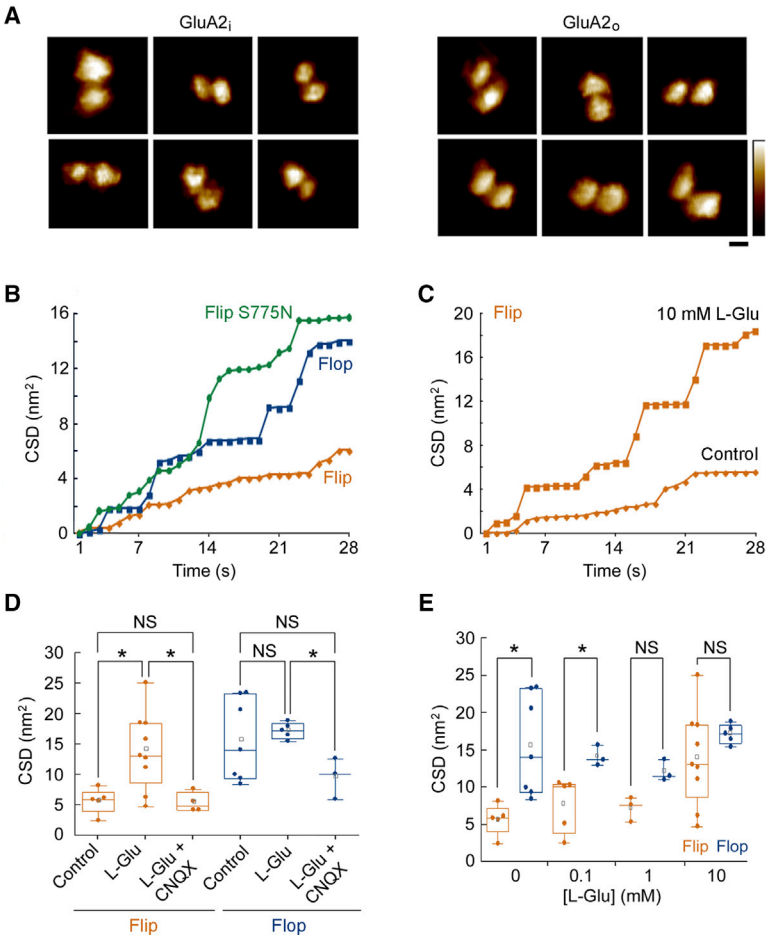

Figure 5. The Mobility of the Resting State of GluA2 AMPA Receptors Is Variable between Flip and Flop Isoforms

(A) Galleries of zoomed (120 × 120 nm) AFM images of individual flip (left) and flop (right) AMPA receptors. Scale bar, 20 nm; color-height scale, 0–8 nm.

(B) Representative cumulative second-by-second (up to 28 s) mobility data for individual flip, flop, and flip S775N AMPA receptors in the resting state.

(C) Representative cumulative second-by-second (up to 28 s) mobility data for individual flip AMPA receptors in the resting state and in the presence of L-Glu (10 mM).

(D) Combined mobility data (at 28 s) for flip and flop AMPA receptors in the resting state, in the presence of L-Glu and in the presence of L-Glu plus CNQX (0.5 mM). Asterisks indicate significant differences ($p < 0.05$) between groups (one-way ANOVA, Fisher's test). NS, not significant.

(E) Combined mobility data (at 28 s) for flip and flop AMPA receptors in the resting state and in the presence of different concentrations of L-Glu. Asterisks indicate significant differences ($p < 0.05$) between flip and flop receptors under equivalent conditions (Mann-Whitney *U* test). CSD, cumulative squared displacement.

See also Table S4 and Videos S1, S2, S3, and S4.

the hypothesis that the flop cassette overrides TARP regulation. Importantly, γ2 also had a greatly attenuated effect on $GluA2_i$ S775N receptors, further demonstrating the pivotal role of the 775 residue as a molecular switch (Figures 6A–6E; Table S1).

Native AMPA Receptors Are Also Sensitive to Anion Regulation

To examine how these actions of the flip/flop cassette impact native receptors, we studied the gating properties of AMPA receptors in outside-out and nucleated patches excised from cerebellar Purkinje and stellate cells, respectively (Figure 7; Table S5). Previous work has shown that AMPA receptors expressed by both cell types are regulated by γ2 but that their gating properties are distinct (Barbour et al., 1994; Bats et al., 2012; Yamazaki et al., 2015). In keeping with this, rapid application (250 ms) of 10 mM L-Glu to excised patches from Purkinje cells elicited AMPA receptor responses that decayed at a slower rate and to a lesser extent than responses from stellate cells (Figure 7A). There was a 6-fold difference in equilibrium desensitization between Purkinje and stellate cells corresponding to steady-state/peak values of 8.3% ± 0.6% (n = 21) and 1.4% ± 0.1% (n = 29), respectively (Figure 7B). Similarly, the decay kinetics of the responses from Purkinje cells were best fit with a weighted time constant of 7.5 ± 0.4 ms (n = 20) compared to 2.9 ± 0.1 ms (n = 30) for responses from stellate cells (Figure 7C). These distinctions in decay kinetics and the degree of equilibrium desensitization of Purkinje and stellate cells are reminiscent of the functional differences between $GluA2_i/\gamma2$ and $GluA2_o/\gamma2$ receptors, respectively (Figures 6A–6D). However, two subsequent observations suggested that a more complicated explanation was required to account for the properties of AMPA receptors expressed by Purkinje and stellate cells.

First, the positive allosteric modulator CTZ (100 μM) eliminated macroscopic desensitization of AMPA receptor-mediated responses of Purkinje and stellate cells (Figure 7A, insets), confirming that both cell types express flip-dominant AMPA receptors (Partin et al., 1994, 1995; Penn et al., 2012). Flop-dominant AMPA receptors continue to desensitize in the presence of CTZ, albeit at a reduced rate (Partin et al., 1994, 1995), which is distinct from the responses observed in patches from Purkinje and stellate cells. Second, although AMPA receptor responses exhibited by Purkinje and stellate cells were sensitive to external anion modulation (Figures 7D and 7E), their effects on decay kinetics were intermediate between $GluA2_i/\gamma2$ and $GluA2_o/\gamma2$ receptor responses (Figure 6D; Table S1). AMPA receptor decay kinetics in both cell types slowed by ~2- to 3-fold upon exchange of external Br^- (Purkinje, $\tau = 3.9 \pm 0.5$ ms, n = 5; stellate, $\tau = 2.0 \pm 0.2$ ms, n = 8) with F^- (Purkinje, $\tau = 10.6 \pm 0.9$ ms, n = 6; stellate, $\tau = 5.0 \pm 0.6$ ms, n = 5). These apparently inconsistent observations may be reconciled if Purkinje and/or stellate cells

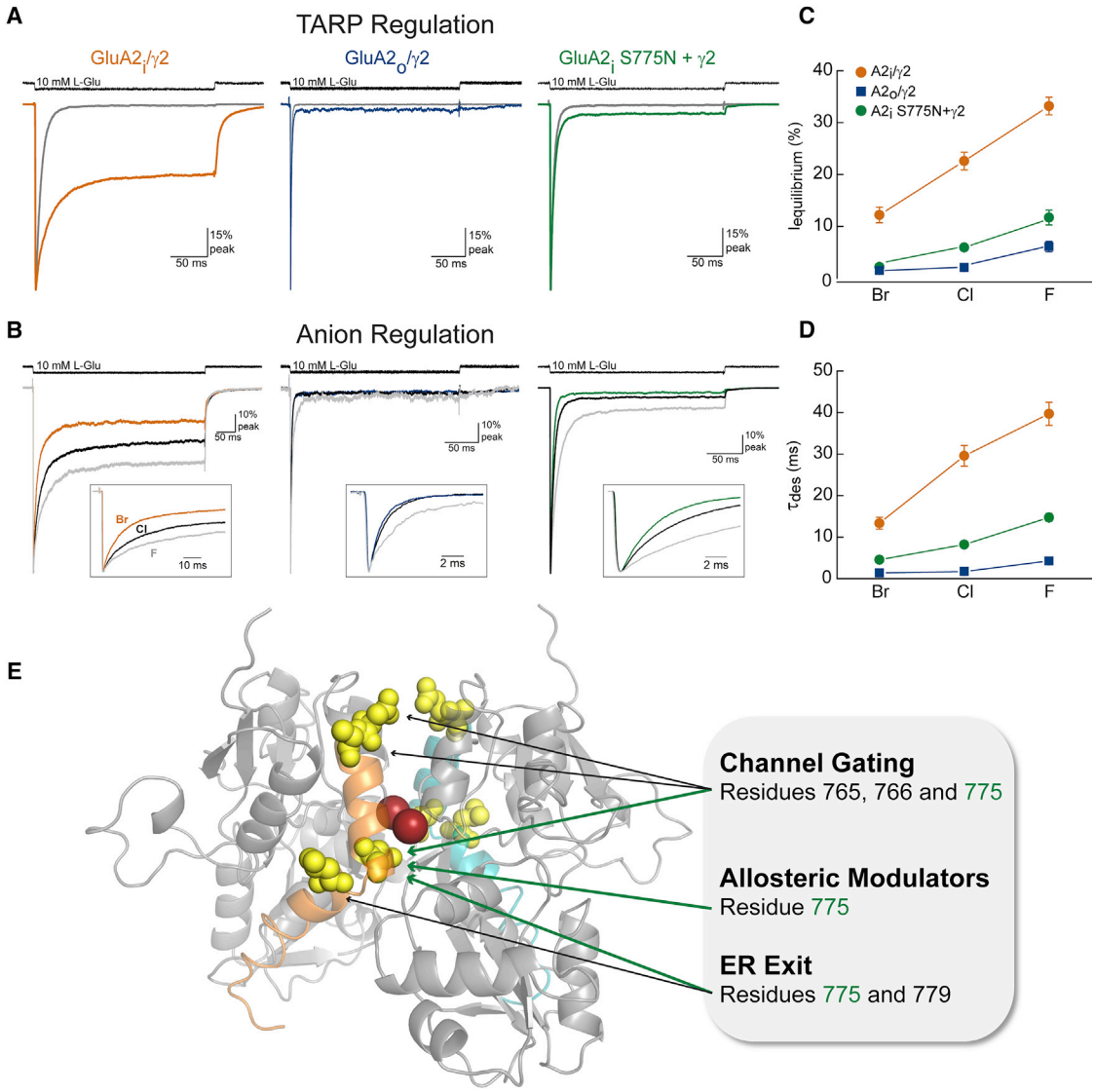

Figure 6. The Flop Cassette Acts as a Master Switch to Override Regulation of AMPA Receptors by TARP Auxiliary Subunits

(A) Typical current responses of $GluA2_i$ (patch 171120p1), $GluA2_o$ (patch 160324p7), and $GluA2_i$ S775N (patch 180813p9) receptors to a 250 ms application of 10 mM L-Glu when co-expressed with γ2 (colored trace). The AMPA receptor responses in the absence of γ2 were taken from patch numbers 180301p3 ($GluA2_i$), 160218p14 ($GluA2_o$), and 160119p3 ($GluA2_i$ S775N). The uppermost trace (black) shows the junction current recorded after the experiment to monitor solution exchange rate.

(B) Typical current responses in different external anions of wild-type and mutant $GluA2_i$ AMPA receptors co-assembled with γ2. ($GluA2_i$, patch 151214p3; $GluA2_o$, patch 160324p7; $GluA2_i$ S775N, patch 180813p9).

(C) Mean equilibrium current amplitude as a percentage of the peak response.

(D) Mean time constants of current decay in the continued presence of L-Glu.

(E) GluA2 LBD dimer highlighting the flip/flop cassette in orange (front) and cyan (back). Although different residues are responsible for the functional differences between flip and flop GluA2 isoforms in terms of channel gating (residues 765, 766, and 775), allosteric regulation by anions and CTZ (residue 775), and ER exit (residues 775 and 779), the 775 residue is implicated in all of these regulatory functions.

See also Table S1.

express AMPA receptor tetramers that contain both flip and flop variants. Consistent with this suggestion, previous work has shown that CTZ eliminates macroscopic desensitization of recombinant $GluA1_i/A2_o$ or $GluA1_o/A2_i$ heteromers (Partin et al., 1994), matching the responses from patches of Purkinje and stellate cells. Since the functional impact of the flip/flop cassette on GluA1/A2 heteromers has yet to be studied in terms of their modulation by TARP γ2 and sensitivity to external anions, we performed additional experiments to better understand this relationship.

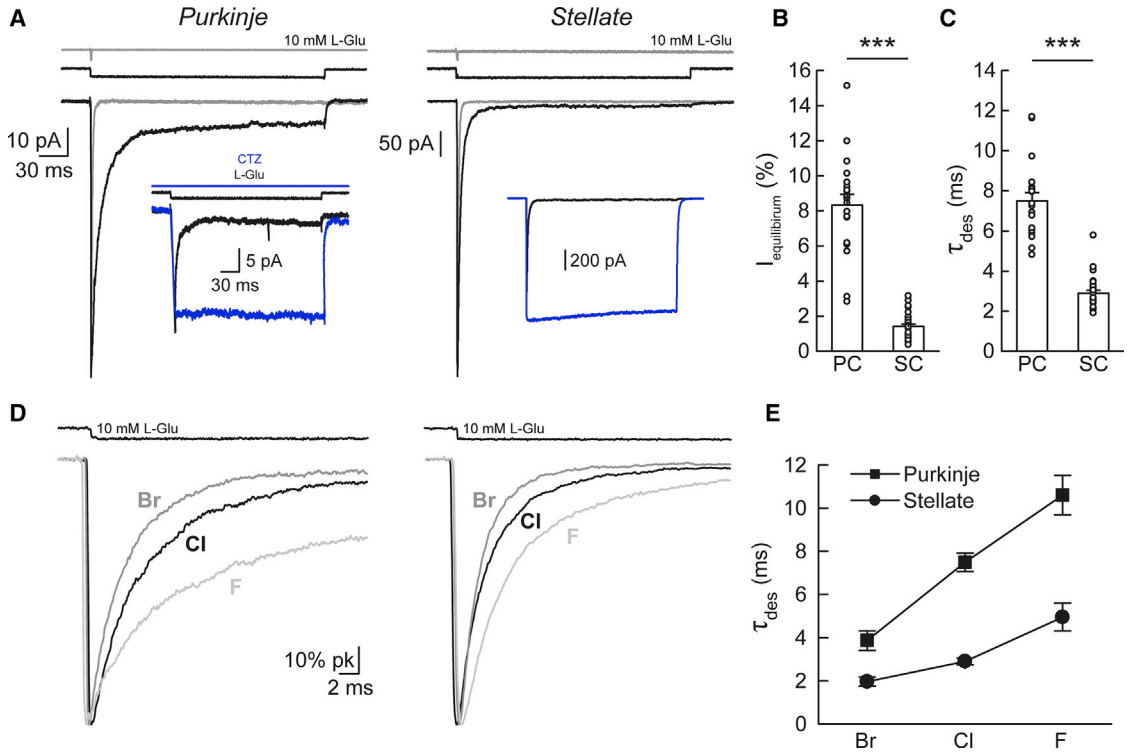

Figure 7. Native AMPA Receptors Are Modulated by External Anions

(A) Typical current responses of an excised Purkinje cell membrane patch (left, patch 190129p5) or stellate cell nucleated patch (right, patch 190205p4) to a 250 ms (black) or 1 ms (gray) application of 10 mM L-Glu. Insets show non-desensitizing responses in the presence of 100 μM CTZ (blue) (Purkinje, patch 190214p8; stellate, patch 190129p3).

(B) Mean equilibrium current amplitude as a percentage of peak response ($I_{equilibrium}$). ***$p < 0.0001$, unpaired t test.

(C) Mean weighted time constants of current decay following 250 ms L-Glu application (τ_{des}). ***$p < 0.0001$, Mann-Whitney *U* test.

(D) Normalized current responses to 250 ms application of L-Glu in NaCl (black), NaBr (dark gray), or NaF (light gray) in Purkinje (left, patch 190213p4) and stellate cell (right, patch 190205p4) patches.

(E) Mean weighted τ_{des} across anion conditions in Purkinje (black squares) and stellate cell (black circles) patches.

Data are presented as mean ± SEM. See also Table S5.

TARP Stoichiometry Shapes the Functional Behavior of AMPA Receptor Heteromers

To examine how alternative splicing impacts the function of GluA1/A2 heteromers, we initially focused on fully TARPed receptors by tethering the γ2 auxiliary subunit to flip/flop variants of GluA1(Q) and GluA2(R) subunits. GluA1/A2 heteromerization was confirmed in each recording by testing for the loss of cytoplasmic polyamine block (Figure S7; see STAR Methods), as described previously (Partin et al., 1995).

The flip/flop cassette had a profound and concomitant effect on the decay kinetics and equilibrium desensitization of fully TARPed GluA1/A2 heteromers (Figure 8A). Flip-only heteromers ($A1_i/\gamma2 + A2_i/\gamma2$) decayed at a slower rate ($\tau = 10.6 \pm 0.3$ ms, n = 6) and to a lesser extent (ss/peak = 18.5% ± 1.4%, n = 6) in response to agonist stimulation than flop-only receptors ($A1_o/\gamma2 + A2_o/\gamma2$), which had faster decay kinetics ($\tau = 3.0 \pm 0.2$ ms, n = 7) and more complete equilibrium desensitization (ss/peak = 3.5% ± 0.8%, n = 7) (Figures 8B–8D; Table S5). Although, GluA1/A2 heteromers containing both flip/flop variants had intermediate behavior, as might be expected, alternative splicing of GluA2 had the more dominant impact on channel gating. For example, $GluA1_i/A2_o$ receptors ($A1_i/\gamma2 + A2_o/\gamma2$) exhibited faster ($\tau = 3.3 \pm 0.3$ ms, n = 7) and more complete desensitization (ss/peak = 7.1% ± 0.7%, n = 7) than $GluA1_o/A2_i$ receptors ($A1_o/\gamma2 + A2_i/\gamma2$, $\tau = 8.9 \pm 0.5$ ms, n = 8; ss/peak = 14.3% ± 1.5%, n = 8) (Figures 8B–8D; Table S5). Analysis of anion effects on fully TARPed GluA1/A2 heteromers revealed a similar relationship, where flip-only heteromers were more sensitive to anion regulation than flop-only heteromers and alternative splicing of GluA2 had the more dominant effect (Figure 8E; Table S5). Interestingly, the decay kinetics and equilibrium desensitization of fully TARPed GluA1/A2 heteromers exhibited a linear relationship across all external anion conditions (Figure 8F). Given this, we reasoned that this relationship could be used to interrogate TARP γ2 stoichiometry of native AMPA receptors with the data already obtained from cerebellar Purkinje and stellate cells.

In keeping with this, anion modulation of native AMPA receptors of cerebellar Purkinje cells was well fit by a linear relationship that was statistically indistinguishable from fully TARPed recombinant GluA1/A2 heteromers (p = 0.10, ANOVA; Figure 8F, red). The data taken from stellate cells, however, did not match the

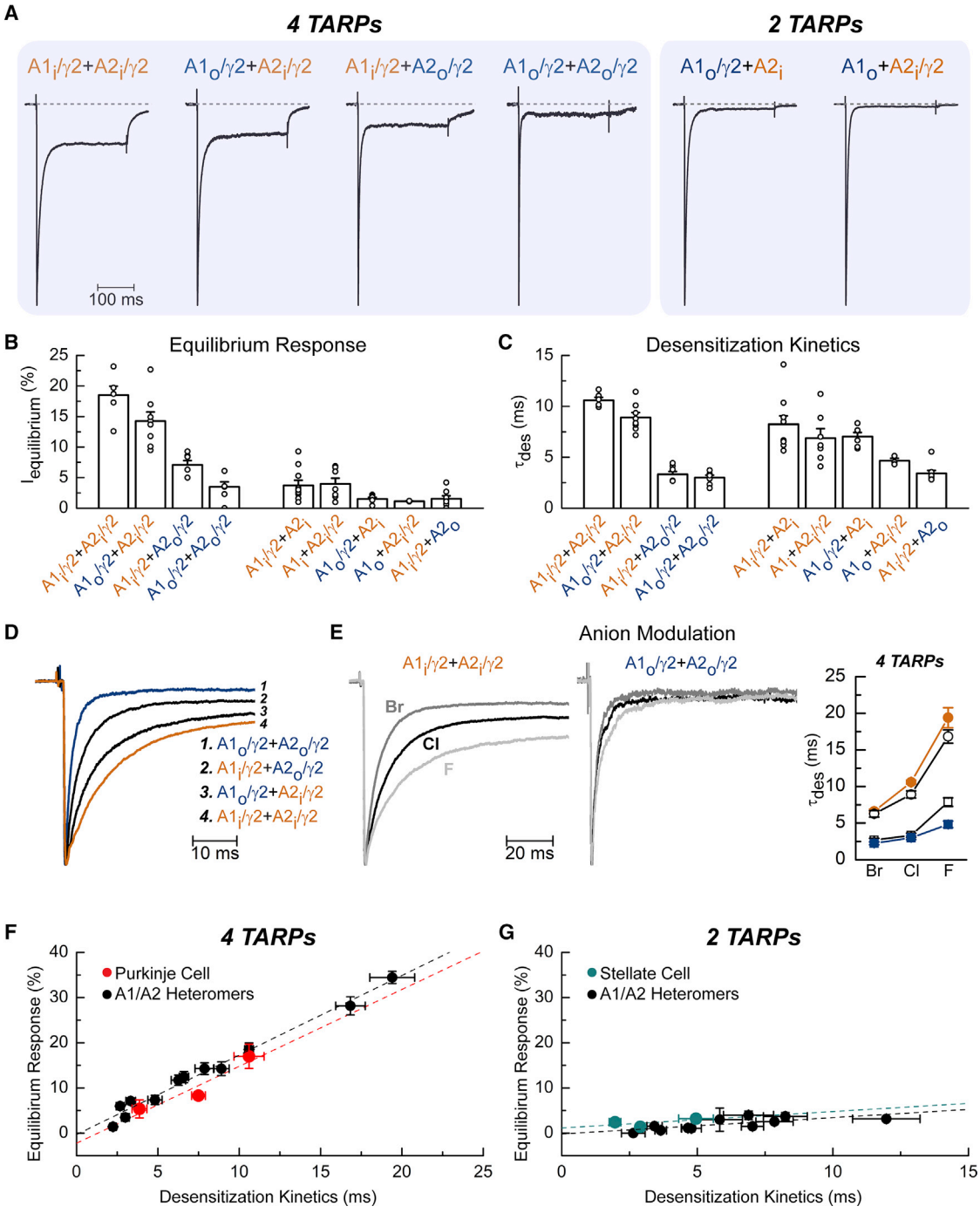

Figure 8. The Functional Behavior of AMPA Receptor Heteromers Is Shaped by TARP Stoichiometry

(A) Typical current responses of heteromeric AMPA receptors to a 250 ms application of 5 mM L-Glu in tandem with TARP γ2 when indicated. Example traces are in the following sequence from left to right: GluA1$_i$/γ2+GluA2$_i$/γ2 (patch 190215p2), GluA1$_o$/γ2+GluA2$_i$/γ2 (patch 190215p13), GluA1$_i$/γ2+GluA2$_o$/γ2 (patch 190228p2), GluA1$_o$/γ2+GluA2$_o$/γ2 (patch 190301p2), GluA1$_o$/γ2+GluA2$_i$ (patch 190213p3), and GluA1$_o$+GluA2$_i$/γ2 (patch 190204p11). All GluA2$_{i/o}$ plasmids are Q/R edited.

(B) Mean equilibrium current amplitude as a percentage of the peak response.

(C) Mean time constants of current decay in the continued presence of L-Glu. Data are presented as mean ± SEM with values of individual patches plotted as white circles.

(D) Overlay of current responses of heteromeric AMPA receptors co-expressed with 4 TARPs (A, left) on a shorter timescale.

(legend continued on next page)

relationship; even though the stellate cell data were well fit by linear regression, the relationship had a different slope (Figure 8G, cyan). Unlike fully TARPed receptors and AMPA receptors from Purkinje cells, equilibrium responses elicited by AMPA receptors from stellate cells were only weakly sensitive to anion modulation (Figure 7; Table S5). Given this, we reasoned that the response profile of AMPA receptors from stellate cells might be more consistent with a partially TARPed receptor.

To test this, we examined the functional behavior of flip/flop variants of GluA1/A2 heteromers in which γ2 was tethered to either the GluA1 or GluA2 subunit so that any GluA1/A2 tetramer combination would possess only two γ2 auxiliary subunits. As anticipated, the relationship between decay kinetics and equilibrium desensitization of partially TARPed GluA1/A2 receptors was different from that of fully TARPed heteromers (Figure 8G). For example, although flip-containing heteromers exhibited slower desensitization kinetics (e.g., $A1_i/\gamma2 + A2_i$, $\tau = 8.2 \pm 0.8$ ms, n = 10) than heteromers containing both flip and flop (e.g., $A1_i/\gamma2 + A2_o$, $\tau = 3.4 \pm 0.3$ ms, n = 8), the degree of equilibrium desensitization was similar in each case ($A1_i/\gamma2 + A2_i$, ss/peak = 3.7% ± 0.9%, n = 10 versus $A1_i/\gamma2 + A2_o$, ss/peak = 1.5% ± 0.5%, n = 8) (Figures 8B and 8C; Table S5). Although partially TARPed heteromers containing both flip/flop variants had intermediate behavior, alternative splicing of GluA2 had the more dominant impact on desensitization kinetics. For example, $GluA1_i/A2_o$ receptors exhibited faster desensitization kinetics ($A1_i/\gamma2 + A2_o$, $\tau = 3.4 \pm 0.3$ ms, n = 8) than $GluA1_o/A2_i$ receptors ($A1_o/\gamma2 + A2_i$, $\tau = 7.0 \pm 0.4$ ms, n = 6) (Figures 8B and 8C; Table S5). Thus, the decay kinetics of partially TARPed AMPA receptors varied according to subunit composition and the external anion type, whereas equilibrium desensitization was relatively unchanged (Figure 8G; Table S5), much like the behavior of AMPA receptors from stellate cells (Figure 7). In fact, linear regression plots of data from partially TARPed AMPA receptors and stellate cells were statistically indistinguishable (p = 0.20, ANOVA; Figure 8G), suggesting that stellate cells express partially TARPed AMPA receptors. Taken together, these data provide compelling evidence for the important role of TARP stoichiometry in dictating the functional behavior of recombinant and native AMPA receptor heteromers. Our results also provide a proof-of-principle approach for future enquiry interrogating the auxiliary subunit composition of native receptors.

DISCUSSION

The present study advances our understanding of a major neurotransmitter receptor in several important ways. First, it underlines the central importance of the apo state in priming the receptor prior to activation and dictating its responsiveness to channel activators, allosteric modulators, and auxiliary proteins. Second, it uncovers an unappreciated and new role of alternative splicing of the flip/flop cassette, which shapes AMPA receptor signaling by regulating the nature of the apo state. Third, it reveals the additional role of TARP stoichiometry in also dictating the functional behavior of AMPA receptor heteromers and its potential value in explaining the responsiveness of native AMPA receptors. Finally, it establishes that the LBD of AMPA receptors exerts a long-range allosteric control on motions in the NTD. As discussed below, differences in the nanoscale mobility of the NTD may affect the trafficking and/or synapse strengthening of different subtypes of native AMPA receptors at glutamatergic synapses.

The Dynamic Nature of the Apo or Resting State

For decades, it has been assumed that the work performed by signaling proteins, such as ion channels, is initiated by the binding energy derived from a plethora of soluble activators, such as neurotransmitters. As a result, the role of the apo or resting state has been largely overlooked. However, some observations, particularly on nicotinic acetylcholine receptors (nAChRs), have challenged this orthodoxy. For example, nAChRs expressed by skeletal muscle can access the open or activated state of the channel in the absence of receptor agonists (Jackson, 1984, 1986), suggesting an underlying dynamic nature to the apo state. The probability that wild-type, unbound nAChRs enter into the open state is small; however, many mutations throughout the protein can increase this probability almost as much as agonist binding (Jadey et al., 2011; Purohit and Auerbach, 2009). In keeping with this, some nAChR mutations associated with congenital myasthenic syndromes can be linked to selective changes in the apo state rather than the activated state (Engel et al., 2010; Jadey et al., 2011), highlighting the importance of the resting state in the context of human disease.

The *lurcher* mutation (A654T) of the delta2 (δ2) iGluR subunit gives rise to cerebellar ataxia (Zuo et al., 1997) and was also concluded to reflect changes in the apo state, since wild-type δ2 iGluRs are unresponsive to neurotransmitter (Hansen et al., 2009; Kohda et al., 2000; Taverna et al., 2000). The homologous mutation is also found in *de novo* missense mutations of GluA1 and GluA3 AMPA receptor subunits, where it is associated with severe neurodevelopmental delay and autism (Geisheker et al., 2017). It was initially proposed that the *lurcher* mutation in GluA1 channels also gives rise to constitutively active channels (Kohda et al., 2000; Schwarz et al., 2001; Taverna et al., 2000); however, a more recent assessment concluded that the mutation has little or no effect on the apo state but rather increases sensitivity to the neurotransmitter L-Glu (Klein and Howe, 2004). The

(E) Left: typical current responses of $GluA1_i/\gamma2$+$GluA2_i/\gamma2$ (patch 190215p2) and $GluA1_o/\gamma2$+$GluA2_o/\gamma2$ (patch 190301p1) in external NaCl (black), NaBr (dark gray), or NaF (light gray). Right: summary of τ_{des} of $GluA1_i/\gamma2$+$GluA2_i/\gamma2$ (orange circles), $GluA1_o/\gamma2$+$GluA2_i/\gamma2$ (white circles), $GluA1_i/\gamma2$+$GluA2_o/\gamma2$ (white squares), and $GluA1_o/\gamma2$+$GluA2_o/\gamma2$ (blue squares) in external NaCl, NaBr, and NaF.
(F and G) Mean equilibrium current percentage plotted against mean time constants of desensitization. (F) GluA1+GluA2 combinations in tandem with 4 TARPs (black circles) are included with pulled patches from cerebellar Purkinje cells (red circles). (G) GluA1+GluA2 combinations in tandem with 2 TARPs (black circles) are included with pulled patches from cerebellar stellate cells (cyan circles). Data were fit by linear regression: (F) black, y = 1.76 − 0.30, r = 0.991; red, y = 1.70 − 2.23, r = 0.948; p = 0.10, one-way ANOVA; (G) black, y = 0.36 − 0.18, r = 0.738; cyan, y = 0.36 + 1.15, r = 0.614; p = 0.20, one-way ANOVA.
See also Table S5.

present study uncovers the existence of functionally distinct apo states of the AMPA receptor that are regulated through alternative splicing of the LBD. Rather than facilitating entry into the main open state, the flip/flop cassette establishes the mobility of the apo state and, in doing so, fine-tunes the responsiveness of AMPA receptors to neurotransmitter, allosteric anions, and auxiliary proteins. As explained below, the complex expression pattern of flip and flop isoforms in the vertebrate brain suggests that the apo or resting state plays a critical role in neuronal signaling of developing and adult neuronal circuits.

A Unifying Role for the AMPA Receptor Flip/Flop Cassette

We identify an entirely new and unifying role for the AMPA receptor flip/flop cassette through its regulation of the apo or resting state of AMPA receptors. Previous studies have linked the flip/flop cassette to several important and apparently disparate properties of AMPA receptors that include determining the rates into AMPA receptor desensitization (Koike et al., 2000; Mosbacher et al., 1994; Quirk et al., 2004), regulation by positive allosteric modulators, such as CTZ, aniracetam, CX614, and PEPA (4-[2-(phenylsulfonylamino)ethylthio]-2,6-difluoro-phenoxyacetamide) (Jin et al., 2005; Partin et al., 1994, 1995; Sekiguchi et al., 1997; Sun et al., 2002), and controlling AMPA receptor secretion from the endoplasmic reticulum (ER) (Coleman et al., 2006; Penn et al., 2008) (Figure 6E).

Markov models describing the effect of alternative splicing on AMPA receptor channel gating and its regulation by allosteric modulators have assumed that the flip/flop cassette impacts AMPA receptors only *after* agonist binding (Koike et al., 2000; Partin et al., 1996). Our data provide an alternative explanation whereby the key events that shape channel gating and allosteric modulation occur *before* agonist binding predetermined by the intrinsic mobility of the apo state. In keeping with this, kinetic differences between flip/flop isoforms are controlled by three closely positioned residues in the flip/flop cassette (Figures 3B and 6E), including Ser775Asn (Quirk et al., 2004). As this same residue regulates the apo state, it establishes a causal link between the mobility of the apo state with channel gating and allosteric modulation.

The effect of alternative splicing on AMPA receptor secretion from the ER has also been associated with motions triggered by agonist-bound AMPA receptors, primarily through the Val/Leu779 residue in coordination with Ser/Asn775 (Coleman et al., 2006; Penn et al., 2012) (Figure 6E). Interestingly, mutating the Thr765 and Pro766 residues of the flip cassette to Asn and Ala in the flop isoform (Figures 3A and 3B) has no effect on AMPA receptor secretion from the ER (Penn et al., 2008) but yet with Ser775Asn, they fully account for the kinetic differences between flip and flop isoforms (Quirk et al., 2004). This distinction reveals that some of the amino acid residues of the flip/flop cassette that govern differences in channel gating and ER exit of AMPA receptors are separable. Importantly, the Ser/Asn775 residue is implicated in all of these known regulatory effects of alternative splicing, which is in keeping with its central structural position at the kink between helices J and K of the flip/flop cassette (Figure 6E) separating the 765/766 residues, which control channel gating, from the 779 residue, which controls ER exit. This structural arrangement has important ramifications for the developing and adult CNS, since the expression of the flip/flop cassette in neurons is developmentally regulated (Monyer et al., 1991), activity dependent (Penn et al., 2012), and cell-type specific (Sommer et al., 1990). Consequently, our work establishes for the first time that fine-tuning nanoscale movements of apo or resting AMPA receptors may be a critical factor governing glutamatergic signaling in the mammalian brain. Finally, whether the nearby arginine of the R/G site, which fits directly into the LBD dimer interface (Greger et al., 2006), could influence LBD stability as well as anion and TARP sensitivity awaits to be studied.

TARP Stoichiometry Dictates the Functional Behavior of Alternatively Spliced AMPA Receptors

Our study establishes that TARP stoichiometry modifies the actions of the flip/flop cassette on recombinant AMPA receptor heteromers, generating two functionally distinct classes that correspond to partially and fully TARPed AMPA receptors (Figures 8F and 8G). Biochemical analysis of AMPA receptors native to the cerebellum has suggested that TARP stoichiometry is fixed (Kim et al., 2010), although it was not possible to determine whether the number of TARPs per AMPA receptor tetramer corresponded to partial (i.e., 1, 2, or 3 TARPs) or full occupancy (i.e., 4 TARPs). Cryoelectron microscopy (cryo-EM) structures and single-molecule imaging studies of AMPA receptors have shown that the makeup of AMPA receptor-TARP complexes can be quite variable, with assemblies containing 1 or 2 (Hastie et al., 2013; Twomey et al., 2016) or 4 (Hastie et al., 2013; Twomey et al., 2017a; Zhao et al., 2016) TARP auxiliary subunits per AMPA receptor tetramer complex (Chen and Gouaux, 2019). Our data from AMPA receptors expressed by cerebellar Purkinje and stellate cells suggest that TARP stoichiometry is variable and, most likely, fixed in each neuronal class, in agreement with a previous study comparing TARP stoichiometry between hippocampal granule and CA1 pyramidal cells (Shi et al., 2009). These conclusions are reliant on the similarity between the data from cerebellar neurons and recombinant GluA1/A2 heteromers. Whether a similar relationship can be extended to GluA2/A3 heteromers, another abundant AMPA receptor composition in the CNS (Bowie, 2012; Henley and Wilkinson, 2016; Jacobi and von Engelhardt, 2017), remains to be determined. Since data from Purkinje and stellate cells are consistent with AMPA receptors being fully and partially occupied by TARPs, respectively, it is possible that CNS neurons may regulate AMPA receptor responsiveness by varying the number of auxiliary subunits per tetramer. Since differences in the duration and amplitude of AMPA receptor-mediated excitatory postsynaptic potentials determines whether postsynaptic neurons operate as integrators of synaptic activity or coincidence detectors (König et al., 1996; Shadlen and Newsome, 1994), it will be interesting in future studies to examine the role of TARP stoichiometry in shaping the complex behavior of neuronal circuits.

Long-Range Allosteric Control of the NTD by the Flip/Flop Cassette

Several studies have reported dynamic motions in the NTD of both AMPA- and kainate-type iGluRs (Dürr et al., 2014; Dutta et al., 2015; Matsuda et al., 2016; Meyerson et al., 2014;

Nakagawa et al., 2005), which have been assumed to be a consequence of agonist binding and receptor desensitization (Dürr et al., 2014; Meyerson et al., 2014; Nakagawa et al., 2005). Our data reveal unexpectedly that motions in the NTD occur in the apo state through long-range control exerted by the flip/flop cassette, which primes the receptor prior to agonist binding (Figure 4) and establishes its intrinsic mobility (Figure 5). This mechanism is distinct from the allosteric coupling described for NMDA-type iGluRs, where it is the NTD that dictates the behavior of the LBD of different GluN2-containing isoforms to determine agonist potency and channel kinetics (Gielen et al., 2009; Yuan et al., 2009). Flip variants promote moderate NTD movement and give rise to slower channel desensitization and robust regulation by anions and auxiliary subunits. The greater mobility imparted by the flop cassette overrides this allosteric regulation and acts as a master switch, presumably by rendering the LBD dimer interface less stable (Dawe et al., 2015). Removal of the NTD has only a modest slowing effect on AMPA receptor gating and allosteric regulation by anions (Table S1); consequently, it still unclear what role, if any, movements in the NTD may fulfill. An attractive possibility is that nanoscale mobility of the NTD controls transsynaptic contact formation at glutamatergic synapses (Elegheert et al., 2016; García-Nafría et al., 2016), permitting AMPA receptor trafficking during synapse strengthening (Díaz-Alonso et al., 2017; Watson et al., 2017), as recently proposed for GluA1 and GluA2 subunits. Given that most native AMPA receptors are either GluA1/A2 or GluA2/A3 heteromers (Bowie, 2012; Henley and Wilkinson, 2016; Jacobi and von Engelhardt, 2017), it will be interesting in future studies to determine how the flip/flop cassette contributes to receptor trafficking and synapse strengthening.

On a broader perspective, the unappreciated role of the apo or resting state may have far-reaching implications for our understanding of the inner workings of many types of signaling proteins, such as other ion channel families, G-protein-coupled receptors (GPCRs), transporters, and kinases. For example, alternative splicing also dramatically impacts the signaling properties of other iGluRs (Regan et al., 2018), as well as many other ligand- and voltage-gated ion channels (Catterall et al., 2005; Kadowaki, 2015; Latorre et al., 2017; Lipscombe and Andrade, 2015; Soreq, 2015). Whether it can also explain the multiplicity of drug action on signaling proteins, such as GPCR-biased agonism and modulation (Lane et al., 2017), also awaits future investigation.

STAR★METHODS

Detailed methods are provided in the online version of this paper and include the following:

SUPPLEMENTAL INFORMATION

Supplemental Information can be found online at https://doi.org/10.1016/j.neuron.2019.03.046.

ACKNOWLEDGMENTS

We would like to thank technician Heidi Peterson for contributing to expression and purification of protein for crystallization studies and MAX-lab (Lund, Sweden) for providing beamtime and help during data collections. We would also like to thank members of the Bowie lab for the critical reading and comments on the manuscript. This work was supported by operating grants from CIHR (D.B.), the Lundbeck Foundation, Danscatt, and Biostruct-X (J.K.), the Biotechnology and Biological Sciences Research Council (J.M.E.), and Newton-Picarte grant DPI-20140080 (N.B. and J.M.E.). A.P. and Y.Y. were supported by NSERC and FRQS masters fellowships, respectively, and G.D. and R.A. were supported by NSERC doctoral fellowships. M.F.K. was supported by a scholarship from the Islamic Development Bank. E.A.S. was supported by a CONICYT-Chile Cambridge Scholarship, and R.V. was supported by the Lundbeck Foundation.

AUTHOR CONTRIBUTIONS

In the Bowie lab, G.B.D., A.M.P., Y.Y., R.P.D.A., and M.A. carried out the electrophysiology experiments, made figures, and analyzed the data. G.B.D., A.M.P., Y.Y., and R.P.D.A. also contributed to the writing of the manuscript. M.R.P.A. generated the constructs for electrophysiology and AFM, made figures, and contributed to the discussions of the manuscript. D.B. conceived of the study, coordinated the experiments between the different labs, and wrote the manuscript. In the Edwardson and Barrera labs, M.F.K., C.N., C.F., and E.A.S. carried out the AFM experiments and analyzed data. N.P.B. designed the AFM experiments and analyzed data. J.M.E. designed the AFM experiments, analyzed data, and contributed to writing the manuscript. In the Kastrup lab, R.V. carried out crystallization of $GluA2_i$ and $GluA2_o$, collected diffraction data, refined structures, analyzed the structures, made figures, and contributed to writing of the manuscript. K.F. was involved in initial crystallization experiments, data collection, and refinements of $GluA2_o$. J.S.K. hypothesized the existence of an anion-binding site in AMPA receptors, participated in data collections, performed the final refinements of the structures, analyzed the structures, made figures, participated in writing of the manuscript, and generally supervised the work.

DECLARATION OF INTERESTS

The authors declare no competing interests.

Received: December 13, 2018
Revised: March 8, 2019
Accepted: March 28, 2019
Published: April 30, 2019

REFERENCES

Adams, P.D., Afonine, P.V., Bunkóczi, G., Chen, V.B., Davis, I.W., Echols, N., Headd, J.J., Hung, L.W., Kapral, G.J., Grosse-Kunstleve, R.W., et al. (2010). PHENIX: a comprehensive Python-based system for macromolecular structure solution. Acta Crystallogr. D Biol. Crystallogr. *66*, 213–221.

Balasuriya, D., Takahashi, H., Srivats, S., and Edwardson, J.M. (2014). Activation-induced structural change in the GluN1/GluN3A excitatory glycine receptor. Biochem. Biophys. Res. Commun. *450*, 1452–1457.

Barbour, B., Keller, B.U., Llano, I., and Marty, A. (1994). Prolonged presence of glutamate during excitatory synaptic transmission to cerebellar Purkinje cells. Neuron *12*, 1331–1343.

Bats, C., Soto, D., Studniarczyk, D., Farrant, M., and Cull-Candy, S.G. (2012). Channel properties reveal differential expression of TARPed and TARPless AMPARs in stargazer neurons. Nat. Neurosci. *15*, 853–861.

Bowie, D. (2002). External anions and cations distinguish between AMPA and kainate receptor gating mechanisms. J. Physiol. *539*, 725–733.

Bowie, D. (2008). Ionotropic glutamate receptors & CNS disorders. CNS Neurol. Disord. Drug Targets *7*, 129–143.

Bowie, D. (2010). Ion-dependent gating of kainate receptors. J. Physiol. *588*, 67–81.

Bowie, D. (2012). Redefining the classification of AMPA-selective ionotropic glutamate receptors. J. Physiol. *590*, 49–61.

Cais, O., Herguedas, B., Krol, K., Cull-Candy, S.G., Farrant, M., and Greger, I.H. (2014). Mapping the interaction sites between AMPA receptors and TARPs reveals a role for the receptor N-terminal domain in channel gating. Cell Rep. *9*, 728–740.

Catterall, W.A., Goldin, A.L., and Waxman, S.G. (2005). International Union of Pharmacology. XLVII. Nomenclature and structure-function relationships of voltage-gated sodium channels. Pharmacol. Rev. *57*, 397–409.

Chen, S., and Gouaux, E. (2019). Structure and mechanism of AMPA receptor - auxiliary protein complexes. Curr. Opin. Struct. Biol. *54*, 104–111.

Chen, V.B., Arendall, W.B., 3rd, Headd, J.J., Keedy, D.A., Immormino, R.M., Kapral, G.J., Murray, L.W., Richardson, J.S., and Richardson, D.C. (2010). MolProbity: all-atom structure validation for macromolecular crystallography. Acta Crystallogr. D Biol. Crystallogr. *66*, 12–21.

Coleman, S.K., Möykkynen, T., Cai, C., von Ossowski, L., Kuismanen, E., Korpi, E.R., and Keinänen, K. (2006). Isoform-specific early trafficking of AMPA receptor flip and flop variants. J. Neurosci. *26*, 11220–11229.

Dawe, G.B., Musgaard, M., Andrews, E.D., Daniels, B.A., Aurousseau, M.R., Biggin, P.C., and Bowie, D. (2013). Defining the structural relationship between kainate-receptor deactivation and desensitization. Nat. Struct. Mol. Biol. *20*, 1054–1061.

Dawe, G.B., Aurousseau, M.R., Daniels, B.A., and Bowie, D. (2015). Retour aux sources: defining the structural basis of glutamate receptor activation. J. Physiol. *593*, 97–110.

Dawe, G.B., Musgaard, M., Aurousseau, M.R.P., Nayeem, N., Green, T., Biggin, P.C., and Bowie, D. (2016). Distinct structural pathways coordinate the activation of AMPA receptor-auxiliary subunit complexes. Neuron *89*, 1264–1276.

Díaz-Alonso, J., Sun, Y.J., Granger, A.J., Levy, J.M., Blankenship, S.M., and Nicoll, R.A. (2017). Subunit-specific role for the amino-terminal domain of AMPA receptors in synaptic targeting. Proc. Natl. Acad. Sci. USA *114*, 7136–7141.

Dingledine, R., Borges, K., Bowie, D., and Traynelis, S.F. (1999). The glutamate receptor ion channels. Pharmacol. Rev. *51*, 7–61.

Dürr, K.L., Chen, L., Stein, R.A., De Zorzi, R., Folea, I.M., Walz, T., Mchaourab, H.S., and Gouaux, E. (2014). Structure and dynamics of AMPA receptor GluA2 in resting, pre-open, and desensitized states. Cell *158*, 778–792.

Dutta, A., Krieger, J., Lee, J.Y., Garcia-Nafria, J., Greger, I.H., and Bahar, I. (2015). Cooperative dynamics of intact AMPA and NMDA glutamate receptors: similarities and subfamily-specific differences. Structure *23*, 1692–1704.

Elegheert, J., Kakegawa, W., Clay, J.E., Shanks, N.F., Behiels, E., Matsuda, K., Kohda, K., Miura, E., Rossmann, M., Mitakidis, N., et al. (2016). Structural basis for integration of GluD receptors within synaptic organizer complexes. Science *353*, 295–299.

Emsley, P., Lohkamp, B., Scott, W.G., and Cowtan, K. (2010). Features and development of Coot. Acta Crystallogr. D Biol. Crystallogr. *66*, 486–501.

Engel, A.G., Shen, X.M., Selcen, D., and Sine, S.M. (2010). What have we learned from the congenital myasthenic syndromes. J. Mol. Neurosci. *40*, 143–153.

Evans, P. (2006). Scaling and assessment of data quality. Acta Crystallogr. D Biol. Crystallogr. *62*, 72–82.

García-Nafría, J., Herguedas, B., Watson, J.F., and Greger, I.H. (2016). The dynamic AMPA receptor extracellular region: a platform for synaptic protein interactions. J. Physiol. *594*, 5449–5458.

Geisheker, M.R., Heymann, G., Wang, T., Coe, B.P., Turner, T.N., Stessman, H.A.F., Hoekzema, K., Kvarnung, M., Shaw, M., Friend, K., et al. (2017). Hotspots of missense mutation identify neurodevelopmental disorder genes and functional domains. Nat. Neurosci. *20*, 1043–1051.

Gielen, M., Siegler Retchless, B., Mony, L., Johnson, J.W., and Paoletti, P. (2009). Mechanism of differential control of NMDA receptor activity by NR2 subunits. Nature *459*, 703–707.

Greger, I.H., Akamine, P., Khatri, L., and Ziff, E.B. (2006). Developmentally regulated, combinatorial RNA processing modulates AMPA receptor biogenesis. Neuron *51*, 85–97.

Greger, I.H., Watson, J.F., and Cull-Candy, S.G. (2017). Structural and functional architecture of AMPA-type glutamate receptors and their auxiliary proteins. Neuron *94*, 713–730.

Hansen, K.B., Naur, P., Kurtkaya, N.L., Kristensen, A.S., Gajhede, M., Kastrup, J.S., and Traynelis, S.F. (2009). Modulation of the dimer interface at ionotropic glutamate-like receptor delta2 by D-serine and extracellular calcium. J. Neurosci. *29*, 907–917.

Hastie, P., Ulbrich, M.H., Wang, H.L., Arant, R.J., Lau, A.G., Zhang, Z., Isacoff, E.Y., and Chen, L. (2013). AMPA receptor/TARP stoichiometry visualized by single-molecule subunit counting. Proc. Natl. Acad. Sci. USA *110*, 5163–5168.

Henley, J.M., and Wilkinson, K.A. (2016). Synaptic AMPA receptor composition in development, plasticity and disease. Nat. Rev. Neurosci. *17*, 337–350.

Herguedas, B., García-Nafría, J., Cais, O., Fernández-Leiro, R., Krieger, J., Ho, H., and Greger, I.H. (2016). Structure and organization of heteromeric AMPA-type glutamate receptors. Science *352*, aad3873.

Herguedas, B., Watson, J.F., Ho, H., Cais, O., Garcia-Nafria, J., and Greger, I.H. (2019). Architecture of the heteromeric GluA1/2 AMPA receptor in complex with the auxiliary subunit TARP γ8. Science. Published online March 14, 2019. https://doi.org/10.1126/science.aav9011.

Herring, B.E., and Nicoll, R.A. (2016). Long-term potentiation: from CaMKII to AMPA receptor trafficking. Annu. Rev. Physiol. *78*, 351–365.

Horning, M.S., and Mayer, M.L. (2004). Regulation of AMPA receptor gating by ligand binding core dimers. Neuron *41*, 379–388.

Jackson, M.B. (1984). Spontaneous openings of the acetylcholine receptor channel. Proc. Natl. Acad. Sci. USA *81*, 3901–3904.

Jackson, M.B. (1986). Kinetics of unliganded acetylcholine receptor channel gating. Biophys. J. *49*, 663–672.

Jackson, A.C., and Nicoll, R.A. (2011). The expanding social network of ionotropic glutamate receptors: TARPs and other transmembrane auxiliary subunits. Neuron *70*, 178–199.

Jacobi, E., and von Engelhardt, J. (2017). Diversity in AMPA receptor complexes in the brain. Curr. Opin. Neurobiol. *45*, 32–38.

Jadey, S.V., Purohit, P., Bruhova, I., Gregg, T.M., and Auerbach, A. (2011). Design and control of acetylcholine receptor conformational change. Proc. Natl. Acad. Sci. USA *108*, 4328–4333.

Jin, R., Clark, S., Weeks, A.M., Dudman, J.T., Gouaux, E., and Partin, K.M. (2005). Mechanism of positive allosteric modulators acting on AMPA receptors. J. Neurosci. *25*, 9027–9036.

Kabsch, W. (2010). Xds. Acta Crystallogr. D Biol. Crystallogr. *66*, 125–132.

Kadowaki, T. (2015). Evolutionary dynamics of metazoan TRP channels. Pflugers Arch. *467*, 2043–2053.

Kim, K.S., Yan, D., and Tomita, S. (2010). Assembly and stoichiometry of the AMPA receptor and transmembrane AMPA receptor regulatory protein complex. J. Neurosci. *30*, 1064–1072.

Klein, R.M., and Howe, J.R. (2004). Effects of the lurcher mutation on GluR1 desensitization and activation kinetics. J. Neurosci. *24*, 4941–4951.

Kohda, K., Wang, Y., and Yuzaki, M. (2000). Mutation of a glutamate receptor motif reveals its role in gating and delta2 receptor channel properties. Nat. Neurosci. *3*, 315–322.

Koike, M., Tsukada, S., Tsuzuki, K., Kijima, H., and Ozawa, S. (2000). Regulation of kinetic properties of GluR2 AMPA receptor channels by alternative splicing. J. Neurosci. *20*, 2166–2174.

König, P., Engel, A.K., and Singer, W. (1996). Integrator or coincidence detector? The role of the cortical neuron revisited. Trends Neurosci. *19*, 130–137.

Krintel, C., Frydenvang, K., Olsen, L., Kristensen, M.T., de Barrios, O., Naur, P., Francotte, P., Pirotte, B., Gajhede, M., and Kastrup, J.S. (2012). Thermodynamics and structural analysis of positive allosteric modulation of the ionotropic glutamate receptor GluA2. Biochem. J. *441*, 173–178.

Krintel, C., Frydenvang, K., Ceravalls de Rabassa, A., Kaern, A.M., Gajhede, M., Pickering, D.S., and Kastrup, J.S. (2014). L-Asp is a useful tool in the purification of the ionotropic glutamate receptor A2 ligand-binding domain. FEBS J. *281*, 2422–2430.

Lane, J.R., May, L.T., Parton, R.G., Sexton, P.M., and Christopoulos, A. (2017). A kinetic view of GPCR allostery and biased agonism. Nat. Chem. Biol. *13*, 929–937.

Latorre, R., Castillo, K., Carrasquel-Ursulaez, W., Sepulveda, R.V., Gonzalez-Nilo, F., Gonzalez, C., and Alvarez, O. (2017). Molecular determinants of BK channel functional diversity and functioning. Physiol. Rev. *97*, 39–87.

Lipscombe, D., and Andrade, A. (2015). Calcium channel CaVα_1 splice isoforms—tissue specificity and drug action. Curr. Mol. Pharmacol. *8*, 22–31.

Matsuda, K., Budisantoso, T., Mitakidis, N., Sugaya, Y., Miura, E., Kakegawa, W., Yamasaki, M., Konno, K., Uchigashima, M., Abe, M., et al. (2016). Transsynaptic modulation of kainate receptor functions by C1q-like proteins. Neuron *90*, 752–767.

Mayer, M.L., and Armstrong, N. (2004). Structure and function of glutamate receptor ion channels. Annu. Rev. Physiol. *66*, 161–181.

McCoy, A.J., Grosse-Kunstleve, R.W., Adams, P.D., Winn, M.D., Storoni, L.C., and Read, R.J. (2007). Phaser crystallographic software. J. Appl. Cryst. *40*, 658–674.

Meyerson, J.R., Kumar, J., Chittori, S., Rao, P., Pierson, J., Bartesaghi, A., Mayer, M.L., and Subramaniam, S. (2014). Structural mechanism of glutamate receptor activation and desensitization. Nature *514*, 328–334.

Monyer, H., Seeburg, P.H., and Wisden, W. (1991). Glutamate-operated channels: developmentally early and mature forms arise by alternative splicing. Neuron *6*, 799–810.

Mosbacher, J., Schoepfer, R., Monyer, H., Burnashev, N., Seeburg, P.H., and Ruppersberg, J.P. (1994). A molecular determinant for submillisecond desensitization in glutamate receptors. Science *266*, 1059–1062.

Möykkynen, T., Coleman, S.K., Semenov, A., and Keinänen, K. (2014). The N-terminal domain modulates α-amino-3-hydroxy-5-methyl-4-isoxazolepropionic acid (AMPA) receptor desensitization. J. Biol. Chem. *289*, 13197–13205.

Nakagawa, T., Cheng, Y., Ramm, E., Sheng, M., and Walz, T. (2005). Structure and different conformational states of native AMPA receptor complexes. Nature *433*, 545–549.

Partin, K.M., Patneau, D.K., and Mayer, M.L. (1994). Cyclothiazide differentially modulates desensitization of alpha-amino-3-hydroxy-5-methyl-4-isoxazolepropionic acid receptor splice variants. Mol. Pharmacol. *46*, 129–138.

Partin, K.M., Bowie, D., and Mayer, M.L. (1995). Structural determinants of allosteric regulation in alternatively spliced AMPA receptors. Neuron *14*, 833–843.

Partin, K.M., Fleck, M.W., and Mayer, M.L. (1996). AMPA receptor flip/flop mutants affecting deactivation, desensitization, and modulation by cyclothiazide, aniracetam, and thiocyanate. J. Neurosci. *16*, 6634–6647.

Penn, A.C., Williams, S.R., and Greger, I.H. (2008). Gating motions underlie AMPA receptor secretion from the endoplasmic reticulum. EMBO J. *27*, 3056–3068.

Penn, A.C., Balik, A., Wozny, C., Cais, O., and Greger, I.H. (2012). Activity-mediated AMPA receptor remodeling, driven by alternative splicing in the ligand-binding domain. Neuron *76*, 503–510.

Plested, A.J., and Mayer, M.L. (2007). Structure and mechanism of kainate receptor modulation by anions. Neuron *53*, 829–841.

Purohit, P., and Auerbach, A. (2009). Unliganded gating of acetylcholine receptor channels. Proc. Natl. Acad. Sci. USA *106*, 115–120.

Quirk, J.C., Siuda, E.R., and Nisenbaum, E.S. (2004). Molecular determinants responsible for differences in desensitization kinetics of AMPA receptor splice variants. J. Neurosci. *24*, 11416–11420.

Regan, M.C., Grant, T., McDaniel, M.J., Karakas, E., Zhang, J., Traynelis, S.F., Grigorieff, N., and Furukawa, H. (2018). Structural mechanism of functional modulation by gene splicing in NMDA receptors. Neuron *98*, 521–529.e3.

Robert, A., Armstrong, N., Gouaux, J.E., and Howe, J.R. (2005). AMPA receptor binding cleft mutations that alter affinity, efficacy, and recovery from desensitization. J. Neurosci. *25*, 3752–3762.

Schneider, C.A., Rasband, W.S., and Eliceiri, K.W. (2012). NIH Image to ImageJ: 25 years of image analysis. Nat. Methods *9*, 671–675.

Schwarz, M.K., Pawlak, V., Osten, P., Mack, V., Seeburg, P.H., and Köhr, G. (2001). Dominance of the lurcher mutation in heteromeric kainate and AMPA receptor channels. Eur. J. Neurosci. *14*, 861–868.

Sekiguchi, M., Fleck, M.W., Mayer, M.L., Takeo, J., Chiba, Y., Yamashita, S., and Wada, K. (1997). A novel allosteric potentiator of AMPA receptors: 4–2-(phenylsulfonylamino)ethylthio–2,6-difluoro-phenoxyaceta mide. J. Neurosci. *17*, 5760–5771.

Shadlen, M.N., and Newsome, W.T. (1994). Noise, neural codes and cortical organization. Curr. Opin. Neurobiol. *4*, 569–579.

Shaikh, S.A., Dolino, D.M., Lee, G., Chatterjee, S., MacLean, D.M., Flatebo, C., Landes, C.F., and Jayaraman, V. (2016). Stargazin modulation of AMPA receptors. Cell Rep. *17*, 328–335.

Shepherd, J.D., and Huganir, R.L. (2007). The cell biology of synaptic plasticity: AMPA receptor trafficking. Annu. Rev. Cell Dev. Biol. *23*, 613–643.

Shi, Y., Lu, W., Milstein, A.D., and Nicoll, R.A. (2009). The stoichiometry of AMPA receptors and TARPs varies by neuronal cell type. Neuron *62*, 633–640.

Sobolevsky, A.I., Rosconi, M.P., and Gouaux, E. (2009). X-ray structure, symmetry and mechanism of an AMPA-subtype glutamate receptor. Nature *462*, 745–756.

Sommer, B., Keinänen, K., Verdoorn, T.A., Wisden, W., Burnashev, N., Herb, A., Köhler, M., Takagi, T., Sakmann, B., and Seeburg, P.H. (1990). Flip and flop: a cell-specific functional switch in glutamate-operated channels of the CNS. Science *249*, 1580–1585.

Soreq, H. (2015). Checks and balances on cholinergic signaling in brain and body function. Trends Neurosci. *38*, 448–458.

Sun, Y., Olson, R., Horning, M., Armstrong, N., Mayer, M., and Gouaux, E. (2002). Mechanism of glutamate receptor desensitization. Nature *417*, 245–253.

Suzuki, Y., Goetze, T.A., Stroebel, D., Balasuriya, D., Yoshimura, S.H., Henderson, R.M., Paoletti, P., Takeyasu, K., and Edwardson, J.M. (2013). Visualization of structural changes accompanying activation of N-methyl-D-aspartate (NMDA) receptors using fast-scan atomic force microscopy imaging. J. Biol. Chem. *288*, 778–784.

Taverna, F., Xiong, Z.G., Brandes, L., Roder, J.C., Salter, M.W., and MacDonald, J.F. (2000). The Lurcher mutation of an alpha-amino-3-hydroxy-5-methyl- 4-isoxazolepropionic acid receptor subunit enhances potency of glutamate and converts an antagonist to an agonist. J. Biol. Chem. *275*, 8475–8479.

Terwilliger, T.C., Grosse-Kunstleve, R.W., Afonine, P.V., Moriarty, N.W., Zwart, P.H., Hung, L.W., Read, R.J., and Adams, P.D. (2008). Iterative model building, structure refinement and density modification with the PHENIX AutoBuild wizard. Acta Crystallogr. D Biol. Crystallogr. *64*, 61–69.

Traynelis, S.F., Wollmuth, L.P., McBain, C.J., Menniti, F.S., Vance, K.M., Ogden, K.K., Hansen, K.B., Yuan, H., Myers, S.J., and Dingledine, R. (2010). Glutamate receptor ion channels: structure, regulation, and function. Pharmacol. Rev. *62*, 405–496.

Turrigiano, G.G. (2017). The dialectic of Hebb and homeostasis. Philos. Trans. R. Soc. Lond. B Biol. Sci. *372*, 20160258.

Twomey, E.C., Yelshanskaya, M.V., Grassucci, R.A., Frank, J., and Sobolevsky, A.I. (2016). Elucidation of AMPA receptor-stargazin complexes by cryo-electron microscopy. Science *353*, 83–86.

Twomey, E.C., Yelshanskaya, M.V., Grassucci, R.A., Frank, J., and Sobolevsky, A.I. (2017a). Channel opening and gating mechanism in AMPA-subtype glutamate receptors. Nature *549*, 60–65.

Twomey, E.C., Yelshanskaya, M.V., Grassucci, R.A., Frank, J., and Sobolevsky, A.I. (2017b). Structural bases of desensitization in AMPA receptor-auxiliary subunit complexes. Neuron *94*, 569–580.e565.

Ursby, T., Unge, J., Appio, R., Logan, D.T., Fredslund, F., Svensson, C., Larsson, K., Labrador, A., and Thunnissen, M.M. (2013). The macromolecular crystallography beamline I911-3 at the MAX IV laboratory. J. Synchrotron Radiat. *20*, 648–653.

Watson, J.F., Ho, H., and Greger, I.H. (2017). Synaptic transmission and plasticity require AMPA receptor anchoring via its N-terminal domain. eLife *6*, e23024.

Winn, M.D., Ballard, C.C., Cowtan, K.D., Dodson, E.J., Emsley, P., Evans, P.R., Keegan, R.M., Krissinel, E.B., Leslie, A.G., McCoy, A., et al. (2011). Overview of the CCP4 suite and current developments. Acta Crystallogr. D Biol. Crystallogr. *67*, 235–242.

Wong, A.Y., Fay, A.M., and Bowie, D. (2006). External ions are coactivators of kainate receptors. J. Neurosci. *26*, 5750–5755.

Yamazaki, M., Le Pichon, C.E., Jackson, A.C., Cerpas, M., Sakimura, K., Scearce-Levie, K., and Nicoll, R.A. (2015). Relative contribution of TARPs γ-2 and γ-7 to cerebellar excitatory synaptic transmission and motor behavior. Proc. Natl. Acad. Sci. USA *112*, E371–E379.

Yuan, H., Hansen, K.B., Vance, K.M., Ogden, K.K., and Traynelis, S.F. (2009). Control of NMDA receptor function by the NR2 subunit amino-terminal domain. J. Neurosci. *29*, 12045–12058.

Zhao, Y., Chen, S., Yoshioka, C., Baconguis, I., and Gouaux, E. (2016). Architecture of fully occupied GluA2 AMPA receptor-TARP complex elucidated by cryo-EM. Nature *536*, 108–111.

Zuo, J., De Jager, P.L., Takahashi, K.A., Jiang, W., Linden, D.J., and Heintz, N. (1997). Neurodegeneration in Lurcher mice caused by mutation in delta2 glutamate receptor gene. Nature *388*, 769–773.

STAR★METHODS

KEY RESOURCES TABLE

REAGENT or RESOURCE	SOURCE	IDENTIFIER
Antibodies		
Mouse monoclonal anti-hemagglutinin antibody	Covance, HA.11 clone 16B12	MMS-101P; RRID: AB_291259
Bacterial and Virus Strains		
E. coli Origami B (DE3)	Novagen	N/A
Chemicals, Peptides, and Recombinant Proteins		
Spermine tetrahydrochloride	Sigma-Aldrich	Cat#S2876 CAS#306-67-2
Cyclothiazide	Tocris Bioscience	Cat#0713 CAS#2259-96-3
BAPTA, tetrasodium salt	Thermo Fisher	Cat#B1214 CAS#126824-24-6
EGTA tetrasodium salt	Sigma-Aldrich	Cat#E9145 CAS#13368-13-3
D-APV	Abcam	Cat#ab120003 CAS# 79055-68-8
L-glutamic acid monosodium salt hydrate	Sigma-Aldrich	Cat#G1626 CAS#142-47-2
ATP disodium salt hydrate	Sigma-Aldrich	Cat#A2383 CAS#34369-07-8
Phenol red solution	Sigma-Aldrich	Cat#P0290 CAS#143-74-8
Penicillin-Streptomycin	Sigma-Aldrich	Cat#P4333
Polyethyleneimine	Sigma-Aldrich	Cat#764604 CAS#9002-98-6
Anti-hemagglutinin agarose	Sigma-Aldrich	Cat#A2095
Complete protease inhibitor cocktail	Sigma-Aldrich	Cat#11697498001
Biotechnology performance certified water	Sigma-Aldrich	Cat#W3513
CHAPS	Sigma-Aldrich	Cat#C9426 CAS#331717-45-4
Hemagglutinin peptide	Sigma-Aldrich	Cat#I2149 CAS#92000-76-5
L-α-phosphatidylcholine	Avanti Polar Lipids	Cat#840053C
1,2-dioleoyl-*sn*-glycero-3-phospho-L-serine	Avanti Polar Lipids	Cat#840035C
Fast Scan silicon AFM probes	Bruker	FASTSCAN-D
CNQX	Tocris Bioscience	Cat#0190 CAS#115066-14-3
Triton X-100	Sigma-Aldrich	Cat#93443 CAS#9002-93-1
Poly(ethylene glycol) 4,000	Sigma-Aldrich	Cat#81240 CAS#25322-68-3
Deposited Data		
Structure of GluA2o-N775S LBD (S1S2J) in complex with glutamate and RbBr, at 1.75 A	This paper	PBD: 6GIV
Structure of GluA2o LBD (S1S2J) in complex with glutamate and NaBr, at 1.95 A	This paper	PBD: 6GL4
Experimental Models: Cell Lines		
Human: HEK293T/17 cells (for electrophysiology)	ATCC	CRL-11268
Human: tsA201 cells (for AFM)	Suzuki et al., 2013	ECACC 96121229
Experimental Models: Organisms/Strains		
Mouse: C57/BL6J	The Jackson Laboratory	RRID: IMSR_JAX:000664
Recombinant DNA		
pRK5-ΔΔGluA1-flip	Dr. M. Mayer, NIH, Maryland, USA	Partin et al., 1995
pRK5-ΔΔGluA1-flop	This Paper	N/A
pRK5-GluA2(Q/R)-flip	Dr. P. Seeburg, Max Planck Institute for Medical Research, Heidelberg, Germany	N/A
pRK5-GluA2(Q/R)-flop	Dr. P. Seeburg, Max Planck Institute for Medical Research, Heidelberg, Germany	N/A

(*Continued on next page*)

Continued

REAGENT or RESOURCE	SOURCE	IDENTIFIER
pRK5-ΔΔGluA1-flip/γ2 tandem	This paper	N/A
pRK5-ΔΔGluA1-flop/γ2 tandem	This paper	N/A
pRK5-GluA2(Q/R)-flip/γ2 tandem	Dawe et al., 2016	N/A
pRK5-GluA2(Q/R)-flop/γ2 tandem	This paper	N/A
pRK5-GluA2(Q)-flip ΔNTD	This paper	N/A
pRK5-GluA2(Q)-flip ΔNTD-eGFP	This paper	N/A
pRK5-GluA2(Q)-flop ΔNTD-eGFP	This paper	N/A
pRK5-GluA2(Q)-L504A-flip	This paper	N/A
pRK5-GluA2(Q)-L504C-flip	This paper	N/A
pRK5-GluA2(Q)-T765N/P766A-flip	This paper	N/A
pRK5-GluA2(Q)-T765N/P766A/S775N-flip	This paper	N/A
pRK5-GluA2(Q)-S775N-flip	This paper	N/A
His_8-GluA2o-LBD, plasmid PET-22B(+)	Dr. M. Mayer, NIH, Maryland, USA	N/A
His_8-GluA2o- N775S-LBD, plasmid PET-22B(+)	Krintel et al., 2012	N/A
Software and Algorithms		
pCLAMP Software	Molecular Devices	https://www.moleculardevices.com
Origin 7.0 and OriginPro 8.5	OriginLab Corporation	https://www.originlab.com
NanoScope Analysis v1.5	Bruker	https://www.bruker.com
SigmaPlot	Systat Software Inc., San Jose, CA	https://systatsoftware.com/products/sigmaplot/
ImageJ	ImageJ, Schneider et al., 2012	https://imagej.nih.gov/ij/index.html
Adrian's FWHM Software (ImageJ Plugin)	ImageJ	https://imagej.nih.gov/ij/plugins/fwhm/
XDS	Kabsch, 2010	http://xds.mpimf-heidelberg.mpg.de/
CCP4i	Winn et al., 2011	https://www.ccp4.ac.uk/ccp4i_main.php
Coot	Emsley et al., 2010	https://www2.mrc-lmb.cam.ac.uk/personal/pemsley/coot/
Phenix	Adams et al., 2010	https://www.phenix-online.org/
PyMOL Molecular Graphics System	Version 1.7.4, Schrödinger, LLC	https://pymol.org/2/

CONTACT FOR REAGENT AND RESOURCE SHARING

Further information and requests for resources and reagents should be directed to and will be fulfilled by the Lead Contact, Derek Bowie (derek.bowie@mcgill.ca).

EXPERIMENTAL MODEL AND SUBJECT DETAILS

Cell Culture

Electrophysiology experiments: human embryonic kidney cells (HEK293T/17) were purchased from ATCC (CRL-11268). These cells constitutively express the simian virus 40 (SV40) large T-antigen and 17 refers to the clone number selected for its high transfectability. Cells were grown at 37°C under 5% CO_2 in Minimum Essential Medium with GlutaMAX (i.e., MEM GlutaMAX) supplemented with 10% fetal bovine serum. The sex of the cell line is not determined.

AFM experiments: tsA201 cells (a subclone of HEK293 cells stably expressing the SV40 large T-antigen, see Suzuki et al., 2013) were grown at 37°C under 5% CO_2 in Dulbecco's Modified Eagle's Medium (DMEM) supplemented with 10% fetal bovine serum, 100 μg/mL streptomycin and 100 units/mL penicillin. The sex of the cell line is not determined.

Mice

All experiments have been approved by the local authorities, were performed in accordance with the guidelines of the Canadian Council on Animal Care and were approved by the Animal Care Committee of McGill University. Wild-type mice with a C57BL/6J background were obtained from Jackson Laboratories (Bar Harbor, USA) and maintained as a breeding colony at McGill University. Both male and female wild-type mice were used for experiments and ranged from postnatal days 18 to 25.

METHOD DETAILS

Recombinant Electrophysiology

HEK293 cells were used to express recombinant GluA1 and/or GluA2 AMPAR subunits for outside-out patch recordings. For GluA2 homomers, the Q/R unedited flip and flop isoforms ($GluA2Q_i$ and $GluA2Q_o$) were used. For GluA1/A2 heteromers, the Q/R edited flip and flop isoforms of GluA2 ($GluA2R_i$ and $GluA2R_o$) were used. Residue numbering includes the signal peptide. Mutant receptors were generated using site-directed mutagenesis. External and internal recording solutions typically contained (in mM): 150 NaX (X = halide ion), 5 HEPES, 0.1 $CaCl_2$, 0.1 $MgCl_2$, and 2% phenol red at pH 7.4, and 115 NaCl, 10 NaF, 5 HEPES, 5 Na_4BAPTA, 0.5 $CaCl_2$, 1 $MgCl_2$, and 10 Na_2ATP at pH 7.4, respectively. For GluA1/A2 heteromer recordings, 30 μM spermine was included in the internal solution; data points were only included when the I/V plot was linear, typical of GluA2(R)-containing AMPARs (Partin et al., 1995) (see Figure S7). Sucrose was supplemented to maintain the osmotic pressure at 300 mOsm. L-Glu was typically applied at 10 mM and CTZ at 100 μM, unless otherwise indicated.

Recording pipettes were composed of borosilicate glass (3-5 MΩ, King Precision Glass, Inc.) coated with dental wax. The reference electrode was connected to the bath via an agar bridge of 3 M KCl. Agonist solutions were applied using a piezo-stack driven perfusion system, and measured solution exchange time was under 400 μs. Series resistances (3-15 MΩ) were routinely compensated by 95%. All recordings were performed using an Axopatch 200B amplifier (Molecular Devices, LLC). Current records were low-pass filtered by an 8-pole Bessel filter at 10 kHz and sampled at 25-50 kHz. Data were acquired using pClamp9 software (Molecular Devices, LLC) and illustrated using Origin 7 (OriginLab Corp.).

Slice Electrophysiology

Slice preparation

Mice were anesthetized with isoflurane and immediately decapitated. A block of cerebellar vermis was rapidly dissected from the mouse head and submerged in ice-cold cutting solution perfused with carbogen gas (95% O_2, 5% CO_2). Cutting solution contains (in mM): 235 sucrose, 2.5 KCl, 1.25 NaH_2PO_4, 28 $NaHCO_3$, 0.5 $CaCl_2$, 7 $MgCl_2$, 28 D-glucose, 1 ascorbic acid, 3 sodium pyruvate (pH 7.4; 305–315 mOsmol/L). The block of vermis was then fastened to a platform, transferred to the slicing chamber and again submerged in ice-cold cutting solution, bubbled with carbogen throughout the remainder of the procedure. Thin slices of cerebellar vermis (300 μm) were obtained with a vibrating tissue sectioner (Leica VT1200; Leica Instruments, Nussloch, Germany). The slices were transferred to oxygenated artificial cerebrospinal fluid (aCSF) and held at room temperature (21°C-23°C) for at least 1 h before recordings were performed. aCSF contained the following (in mM): 125 NaCl, 2.5 KCl, 1.25 NaH_2PO_4, 26 $NaHCO_3$, 2 $CaCl_2$, 1 $MgCl_2$, 25 D-glucose (pH of 7.4; 305–315 mOsmol/L).

Acute slice electrophysiology

Slice experiments were performed on an Olympus BX51 upright microscope (Olympus, Southall, UK) equipped with differential interference contrast/infrared optics. Recordings were made from either visually identified stellate or Purkinje cells in acute sagittal slices of cerebellar vermis. Patch pipettes were prepared from thick-walled borosilicate glass (GC150F-10, OD 1.5 mm, ID 0.86 mm; Harvard Apparatus Ltd, Kent, UK) and had open tip resistances of 3–6 MΩ when filled with an intracellular recording solution. Internal solution contained (in mM): 140 CsCl, 10 HEPES, 10 EGTA, 2 $MgCl_2$ and 60 μM spermine-HCl to examine rectification due to polyamine channel block (pH of 7.4; 295-305 mOsmol/L). Local agonist/antagonist applications were performed using a homemade flowpipe from theta tubing with a tip diameter of 300–400 μm. External solution was the same as described above with the addition of 10 μM D-APV to block NMDA receptors. Nucleated (stellate) or excised membrane (Purkinje) patches were placed near the mouth of a double-barreled flowpipe, which was rapidly jumped between control and solution containing 10 mM L-Glu (1 - 250 ms duration). Recordings were performed using a Multiclamp 700A amplifier (Molecular Devices, Sunnyvale, CA, USA). The bath was continuously perfused at room temperature (21–23°C) with aCSF at a rate of 1–2 mL/min. Currents were filtered at 5 kHz with an eight-pole low-pass Bessel filter (Frequency Devices, Haverhill, MA, USA) and digitized at 25 kHz with a Digidata 1322A data acquisition board and Clampex 10.1 (pClamp) software.

Crystallization

Wild-type $GluA2_o$ and N775S (flip-like) mutant ligand binding domains (LBDs) were expressed and purified as described previously (Krintel et al., 2012). Crystallization was performed using the vapor diffusion hanging drop method at 6°C. The crystallization drop consisted of 1 μL $GluA2_o$-LBD solution (8 mg/ml) or $GluA2_o$-LBD N775S mutant (4 mg/ml) in a buffer containing 10 mM HEPES, 20 mM NaCl, 1 mM EDTA (pH 7.0), and 1 μL of reservoir solution. Before setting up the crystallization drops, the protein solution was mixed with L-Glu to a final concentration of 2 mM L-Glu and 300 mM NaBr ($GluA2_o$-LBD) or 4 mM L-Glu and 250 mM RbBr ($GluA2_o$-LBD N775S). Crystals used for diffraction data collections were obtained at conditions consisting of reservoir solution: 25% PEG4000, 0.2 M Na_2SO_4, and 0.1 M CH_3COONa, pH 5.5 ($GluA2_o$) or 22%–24% PEG4000, 0.2-0.3 M Li_2SO_4 and 0.1 M cacodylate, pH 6.5 ($GluA2_o$-LBD N775S). Before data collection, the crystals were cryo-protected in reservoir solution containing 20% glycerol.

Data collection and structure determination

X-ray diffraction data on GluA2-LBD crystals were collected at the Max-Lab beamline I911-3 (Lund, Sweden) (Ursby et al., 2013) at 100 K. Diffraction images were processed in XDS (Kabsch, 2010). Data were scaled and merged using SCALA (Evans, 2006) within CCP4 (Winn et al., 2011) and the structures were solved by molecular replacement in Phaser (McCoy et al., 2007) using GluA2-LBD structures as search models (PDB: 3TDJ, molA for $GluA2_o$, (Krintel et al., 2012) and PDB: 4O3A, molA for $GluA2_o$-LBD N775S, (Krintel et al., 2014)). Initially, the structures were rebuilt in AutoBuild (Terwilliger et al., 2008) within Phenix (Adams et al., 2010). Structures were further improved using Coot (Emsley et al., 2010) and refinement in Phenix. Both structures displayed good quality indicators as calculated by MolProbity (Chen et al., 2010) within Phenix. Figures were prepared with the PyMOL Molecular Graphics System (Version 1.7.4, Schrödinger, LLC). For statistics on data collection and refinements, see Table S2.

AMPA receptor purification and AFM imaging

The following constructs were used, all with an HA tag at the N terminus and in the vector pRK5: rat $GluA2_i$ and $GluA2_o$ (Q/R site unedited), $GluA2_i$ with the point mutation S775N, ΔNTD-$GluA2_i$ (minus NTD), ΔNTD $GluA2_i$-GFP and ΔNTD $GluA2_o$-GFP. The HA tag contained the residues YPYDVPDYA, located after the first amino acid following the signal peptide (i.e., between residues 22 and 32).

Isolation of AMPARs

DNA (250 μg) was used to transfect 5 × 162 cm^2 flasks of tsA201 cells using polyethylenimine. After transfection, cells were incubated for 24-48 h at 37°C to allow expression of receptors. Proteins were isolated from transfected cells by immunoaffinity chromatography; all steps were carried out at 4°C. Cell pellets were resuspended in solubilization buffer [25 mM Tris-HCl, pH 7.5, 150 mM NaCl, 10 mM EDTA, 1% Triton X-100, 1 mM PMSF, and protease inhibitor cocktail (Roche), prepared in Biotechnology Performance Certified (BPC) water (Sigma)]. Precipitated DNA was removed by low-speed centrifugation, and the sample was then centrifuged in a 70 Ti rotor at 35,000 rpm for 1 h. Solubilized extracts were incubated with anti-HA-agarose beads (Sigma) for 3 h. The immunobeads bearing captured protein were then washed extensively with solubilization buffer containing 0.1% CHAPS (Sigma) instead of 1% (v/v) Triton X-100, and the bound protein was eluted with HA peptide (200 μg/mL). Protein purity was evaluated by silver staining and immunoblotting.

Integration of receptors into liposomes

Chloroform solutions of L-α-phosphatidylcholine (PC) and 1,2-dioleoyl-sn-glycero-3-phospho-L-serine (DOPS; Avanti Polar Lipids) were mixed at a molar ratio of 3:1. The chloroform was then evaporated under a stream of nitrogen gas, and the lipids were resuspended in HEPES-buffered saline (HBS; 150 mM NaCl, 20 mM HEPES, pH 7.6) containing CHAPS and mixed with purified receptor to give a final lipid concentration of 2 mg/mL and a final CHAPS concentration of 1% (w/v). The mixture was dialysed at 4°C against detergent-free buffer for 2 days, with several changes of buffer. To detect receptors, where appropriate, the dialysed sample was incubated for 12 h at 4°C with anti-HA antibody.

AFM imaging

A droplet (20 μL) of proteoliposome suspension was deposited onto the surface of a freshly cleaved mica disc (diameter, 1 cm), followed by incubation for 5 min at room temperature (20°C), during which time the proteoliposomes collapsed to form supported lipid bilayers containing integrated receptors. The mica surface was gently washed several times with HBS to remove unadsorbed proteoliposomes. AFM imaging under fluid was carried out at room temperature using a Bruker-AXS FastScan Dimension AFM instrument. The instrument was used in micro-volume fluid mode to facilitate the application of agonist, antagonist or ions directly while imaging. All images were collected in 'tapping' mode, using FastScan-D silicon probes (Bruker). The cantilevers (with a typical spring constant of 0.25 N/m) were tuned to a resonance frequency of between 90 and 140 kHz. The microscope was engaged with a 2 μm x 2 μm scan area and a 5 nm target amplitude to allow for tuning. The amplitude setpoint was adjusted to the highest setting that allowed imaging with little noise, to minimize the force applied to the sample. To measure receptor heights, images were captured at a scan rate of 20 Hz (25 s/frame) with 512 scan lines per area. Individual particles were identified, and particles with heights between 5 and 10 nm were taken to represent AMPARs.

To follow the dynamics of the NTDs, sequential high-magnification (120 nm x 120 nm) images of receptor-containing bilayers were captured at a frequency of 1 frame/second with a fixed integral gain of 2.5 and a target amplitude of 1 nm. The target amplitude was kept at 1 nm to exert minimum force on the receptor. Individual particles were identified, and particles with heights between 7 and 10 nm were taken to represent AMPARs. N.B. The particles were slightly taller when using target amplitude 1 nm instead of the conventional target amplitude of 5 nm. Movement of the two globular structures relative to each other was followed under various conditions. The centers of the structures were identified by using Gaussian fitting (ImageJ plug-in, Adrian's FWHM), and NTD mobility was expressed as the cumulative squared displacement (CSD):

$$CSD(t) = \sum_{i=1}^{t} (x_{i+1} - x_i)^2$$

where *x* is the distance between the centers of the globular structures.

Data analysis

Image analysis was performed using the Nanoscope analysis 1.5 software and ImageJ (Schneider et al., 2012). Data analysis was carried out using Microsoft Excel, OriginPro 8.5 or SigmaPlot 12.5. Histograms were drawn with bin widths chosen according to Scott's equation:

$$h = 3.5\sigma / n^{1/3}$$

where *h* is the bin width, σ is an estimate of the standard deviation and *n* is the sample size.

QUANTIFICATION AND STATISTICAL ANALYSIS

Additional details of data analysis and statistical analysis can be found in the Method Details, main and supplemental figures, supplemental tables, and corresponding legends.

Electrophysiological data

Electrophysiological data were analyzed using Clampfit 10.5 (Molecular Devices, LLC). To measure deactivation and entry into desensitization, current decay rates were fitted using 1st or 2nd order exponential functions of the form $y = A_i*\exp(-x/\tau_i)$. Where two exponential components were used, time constants are expressed as a weighted mean. To measure recovery from desensitization, a two-pulse protocol was delivered using variable interpulse intervals, and the peak amplitude of the second pulse was expressed as a fraction of the first peak. Recovery data were fitted with the Hodgkin-Huxley equation $y = N_0+(1-N_0)*(1-\exp(-k_{rec}*x))\text{^}n$, where N_0 is the equilibrium response at the end of the first pulse, k_{rec} is the recovery rate, and n is an exponent that reflects the number of kinetic transitions contributing to the recovery time course. The value of n was set to 2 (see Robert et al., 2005). Distributions were first evaluated using Kolmogorov-Smirnova test. Non-normally distributed data were analyzed using non-parametric tests such as the Mann-Whitney U test where indicated. Normally distributed data were compared using one-way ANOVA and unpaired two-tailed Student's t test. Significance is defined as $p < 0.05$. Data are presented as mean ± SEM, with n referring to individual patches.

Atomic force microscopy data

Data are presented as mean ± SEM, with n referring to individual receptors. Heights of individual AMPARs before and after either the addition of L-Glu or an anion switch were compared using a Student's paired, two-tailed t test. ATD mobility data for flip and flop AMPARs in the resting state, in the presence of L-Glu, and in the presence of L-Glu plus CNQX were compared using a one-way ANOVA, with a Fisher test. Combined ATD mobility data for flip and flop AMPARs in the resting state and in the presence of different concentrations of L-Glu were compared using a Mann-Whitney U test.

DATA AND SOFTWARE AVAILABILITY

The X-ray crystal structures of $GluA2_o$-LBD (PDB: 6GL4) and the flip-like mutant $GluA2_o$-LBD N775S (PDB: 6GIV) have been uploaded to the Protein Data Bank.

Neuron, Volume *102*

Supplemental Information

Nanoscale Mobility of the Apo State and TARP Stoichiometry Dictate the Gating Behavior of Alternatively Spliced AMPA Receptors

G. Brent Dawe, Md. Fahim Kadir, Raminta Venskutonytė, Amanda M. Perozzo, Yuhao Yan, Ryan P.D. Alexander, Camilo Navarrete, Eduardo A. Santander, Marika Arsenault, Christian Fuentes, Mark R.P. Aurousseau, Karla Frydenvang, Nelson P. Barrera, Jette S. Kastrup, J. Michael Edwardson, and Derek Bowie

Figure S1

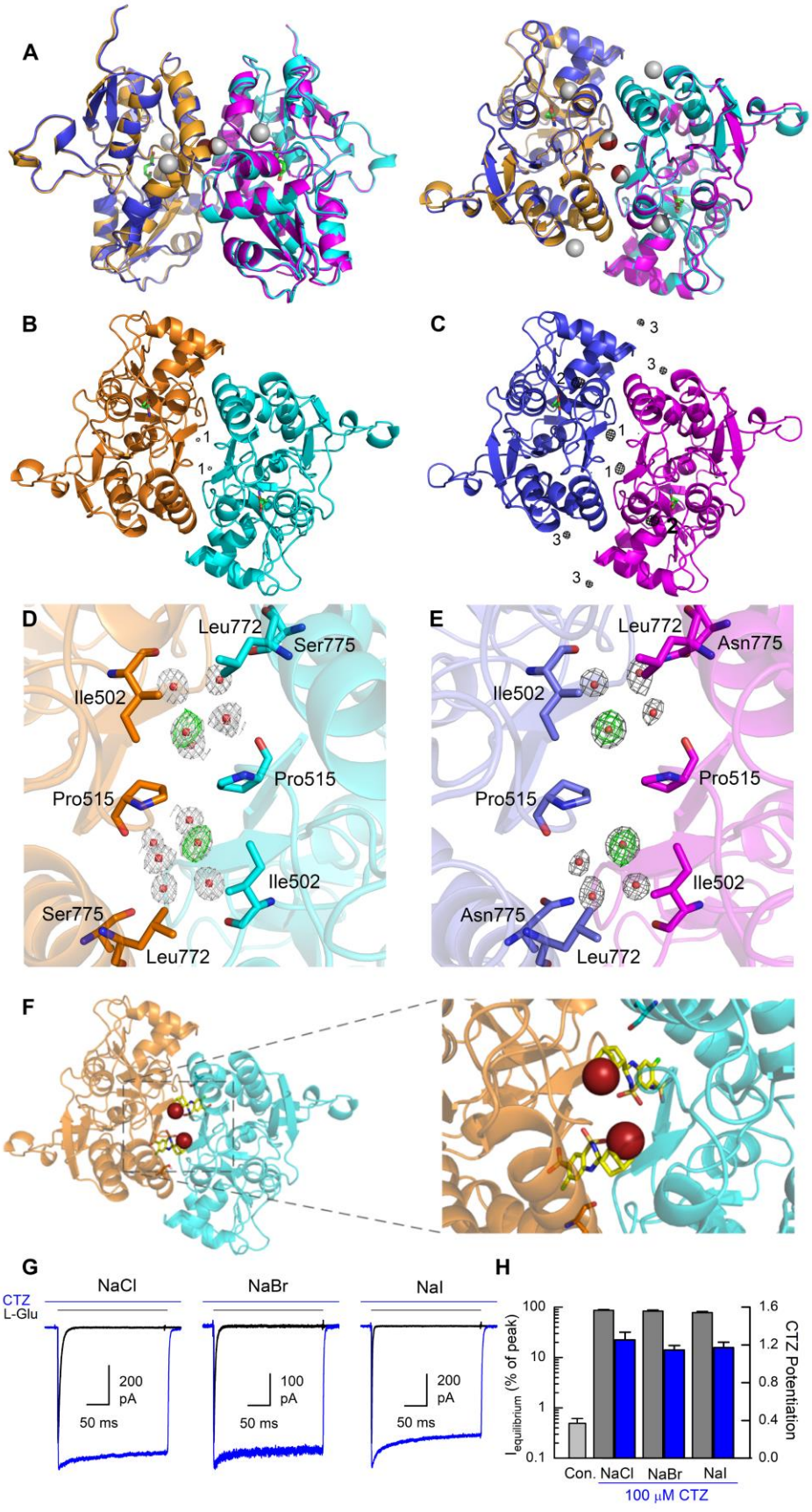
A
B
C
D
Leu772
Ser775
Ile502
Pro515
Pro515
Ile502
Ser775
Leu772
E
Leu772
Asn775
Ile502
Pro515
Pro515
Ile502
Asn775
Leu772
F
G
NaCl
NaBr
NaI
CTZ
L-Glu
200 pA
50 ms
100 pA
50 ms
200 pA
50 ms
H
100
10
1
0.1
1.6
1.2
0.8
0.4
0.0
CTZ Potentiation
Con.
NaCl
NaBr
NaI
100 μM CTZ

Figure S2

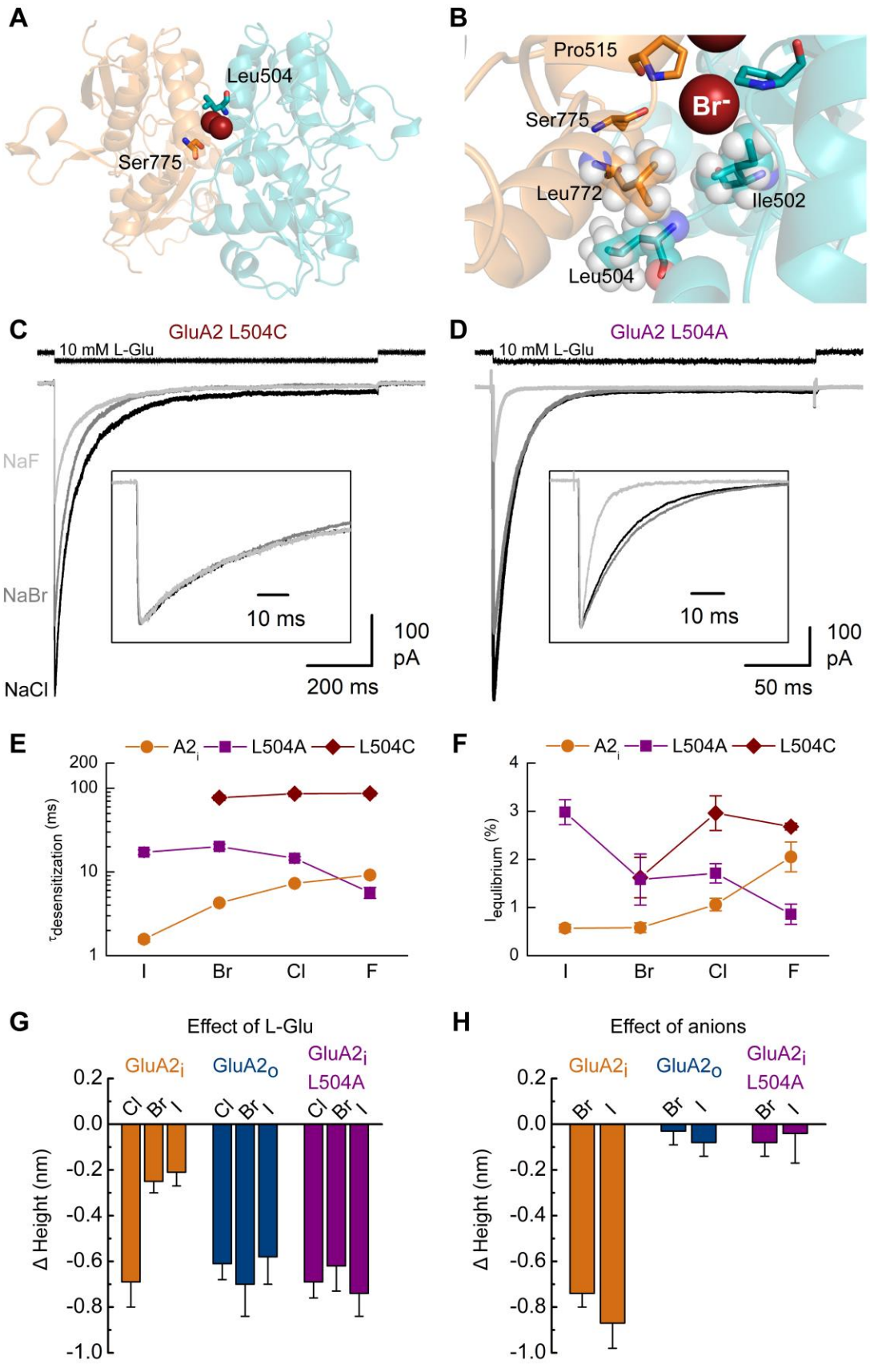
A
Leu504
Ser775
B
Pro515
Br-
Ser775
Leu772
Ile502
Leu504
C
GluA2 L504C
10 mM L-Glu
NaF
NaBr
NaCl
10 ms
100 pA
200 ms
D
GluA2 L504A
10 mM L-Glu
10 ms
100 pA
50 ms
E
A2i
L504A
L504C
τdesensitization (ms)
200
100
10
1
I
Br
Cl
F
F
A2i
L504A
L504C
Iequilibrium (%)
4
3
2
1
0
I
Br
Cl
F
G
Effect of L-Glu
GluA2i
GluA2o
GluA2i L504A
Cl
Br
I
Δ Height (nm)
0.2
0.0
-0.2
-0.4
-0.6
-0.8
-1.0
H
Effect of anions
GluA2i
GluA2o
GluA2i L504A
Br
I
Δ Height (nm)
0.2
0.0
-0.2
-0.4
-0.6
-0.8
-1.0

Figure S3

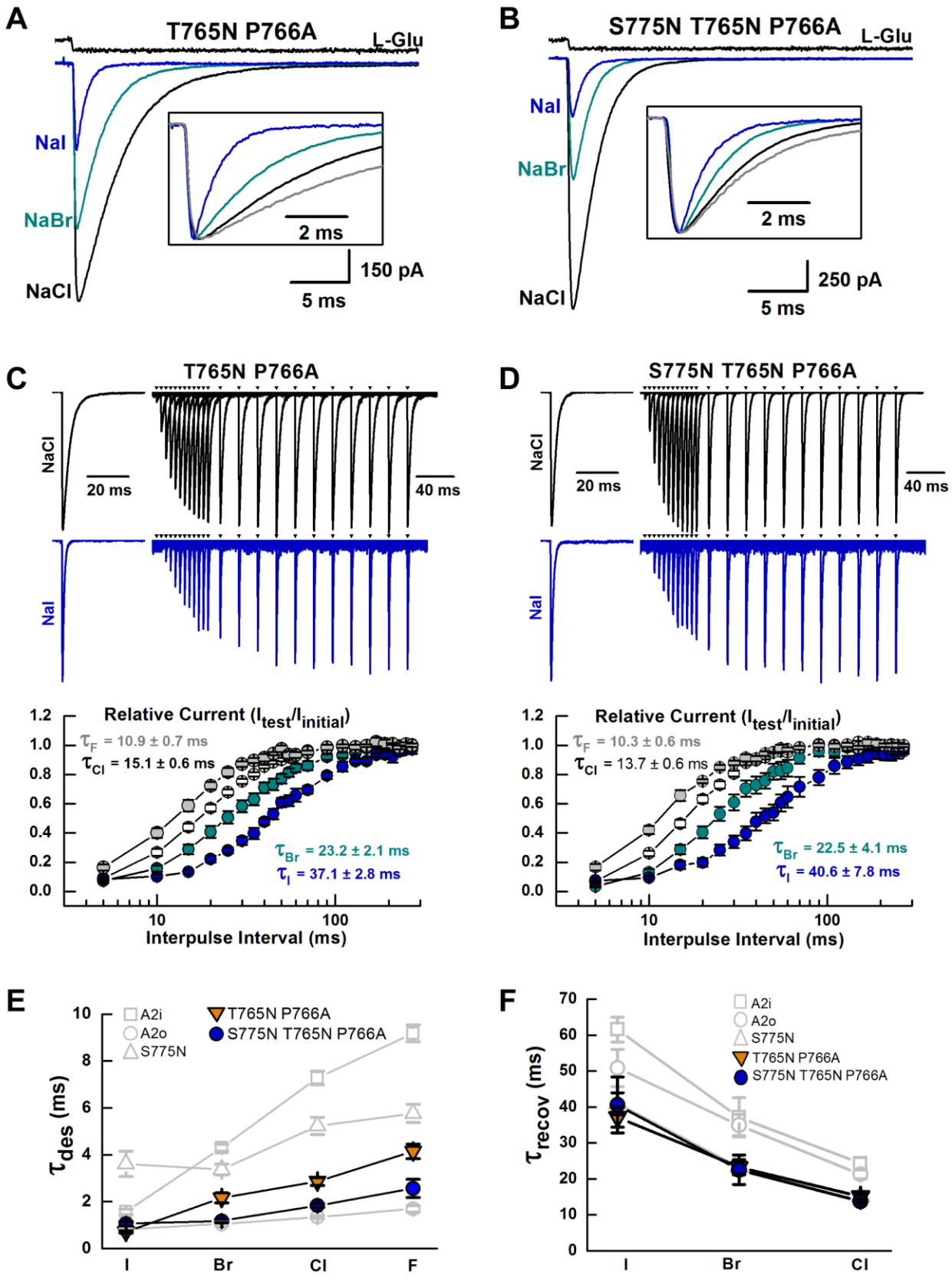
A
T765N P766A
L-Glu
NaI
NaBr
NaCl
2 ms
150 pA
5 ms
B
S775N T765N P766A
L-Glu
NaI
NaBr
NaCl
2 ms
250 pA
5 ms
C
T765N P766A
NaCl
20 ms
40 ms
NaI
Relative Current (I_test/I_initial)
τ_F = 10.9 ± 0.7 ms
τ_Cl = 15.1 ± 0.6 ms
τ_Br = 23.2 ± 2.1 ms
τ_I = 37.1 ± 2.8 ms
Interpulse Interval (ms)
D
S775N T765N P766A
NaCl
20 ms
40 ms
NaI
Relative Current (I_test/I_initial)
τ_F = 10.3 ± 0.6 ms
τ_Cl = 13.7 ± 0.6 ms
τ_Br = 22.5 ± 4.1 ms
τ_I = 40.6 ± 7.8 ms
Interpulse Interval (ms)
E
A2i
A2o
S775N
T765N P766A
S775N T765N P766A
τ_des (ms)
I
Br
Cl
F
F
A2i
A2o
S775N
T765N P766A
S775N T765N P766A
τ_recov (ms)
I
Br
Cl

Figure S4

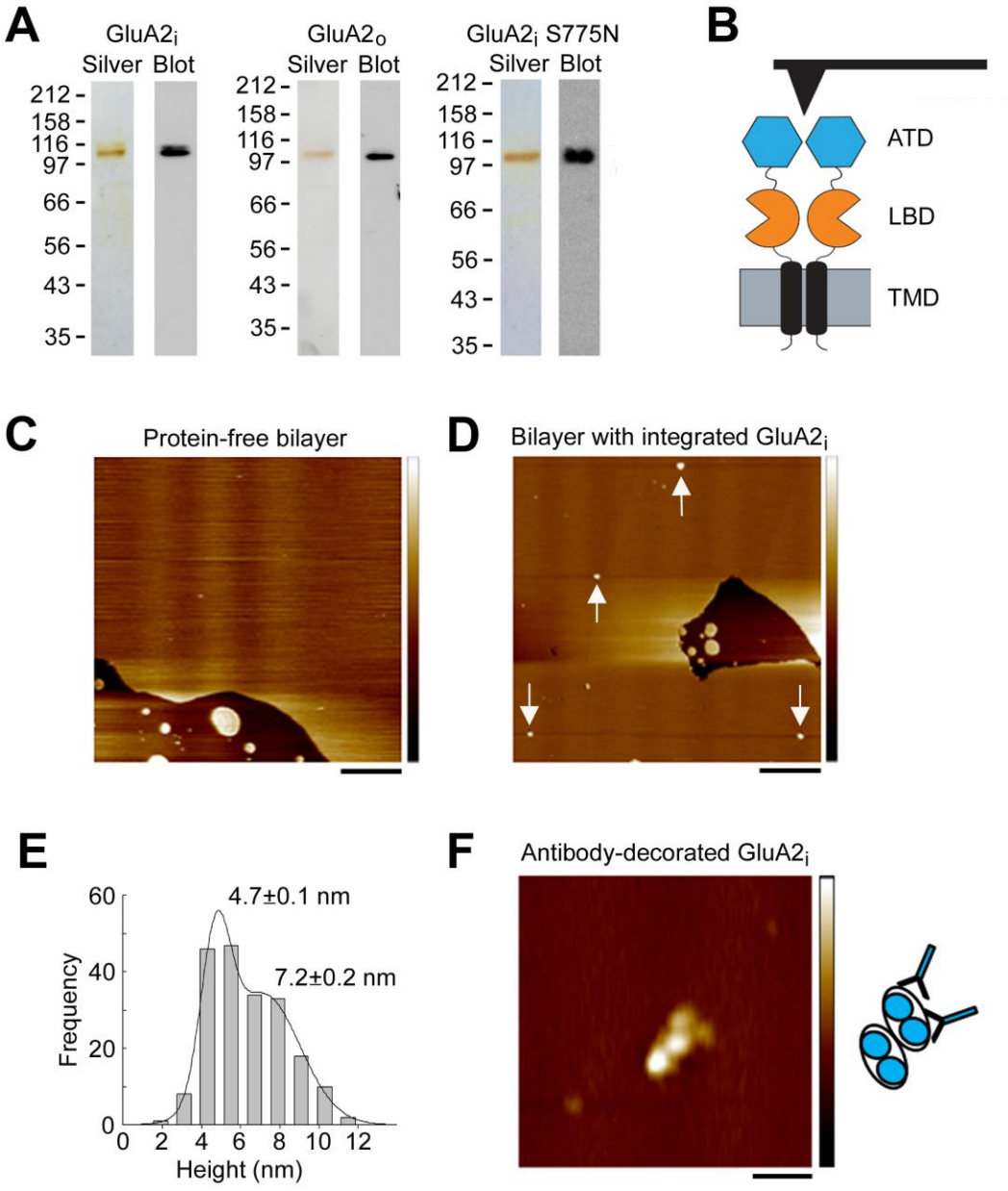
A
GluA2i
Silver Blot
GluA2o
Silver Blot
GluA2i S775N
Silver Blot
212
158
116
97
66
56
43
35
B
ATD
LBD
TMD
C
Protein-free bilayer
D
Bilayer with integrated GluA2i
E
4.7±0.1 nm
7.2±0.2 nm
Frequency
Height (nm)
F
Antibody-decorated GluA2i

Figure S5

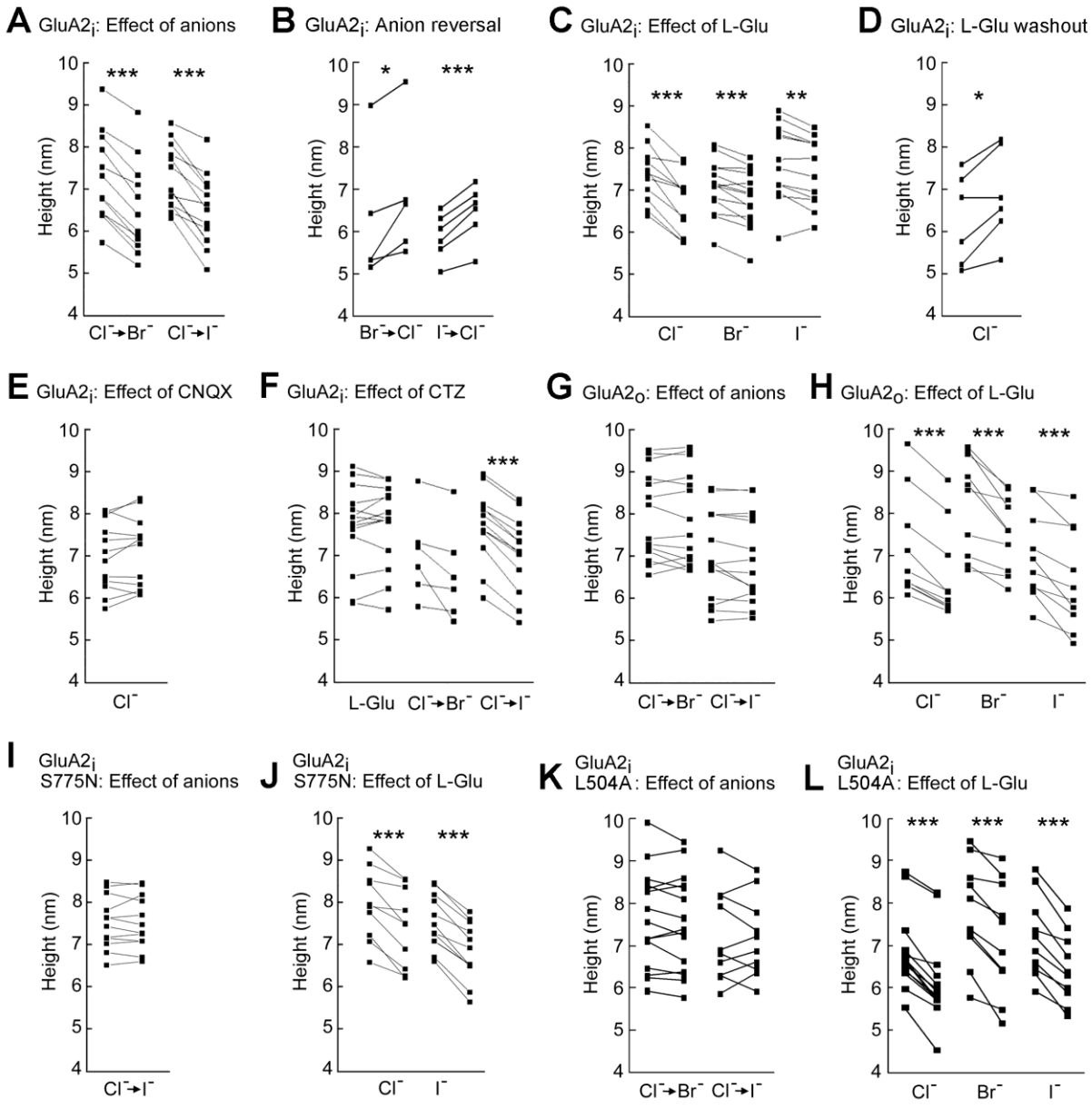
A GluA2i: Effect of anions
B GluA2i: Anion reversal
C GluA2i: Effect of L-Glu
D GluA2i: L-Glu washout
E GluA2i: Effect of CNQX
F GluA2i: Effect of CTZ
G GluA2o: Effect of anions
H GluA2o: Effect of L-Glu
I GluA2i S775N: Effect of anions
J GluA2i S775N: Effect of L-Glu
K GluA2i L504A: Effect of anions
L GluA2i L504A: Effect of L-Glu
Height (nm)
Cl⁻→Br⁻
Cl⁻→I⁻
Br⁻→Cl⁻
I⁻→Cl⁻
Cl⁻
Br⁻
I⁻
L-Glu
*
**
***

Figure S6

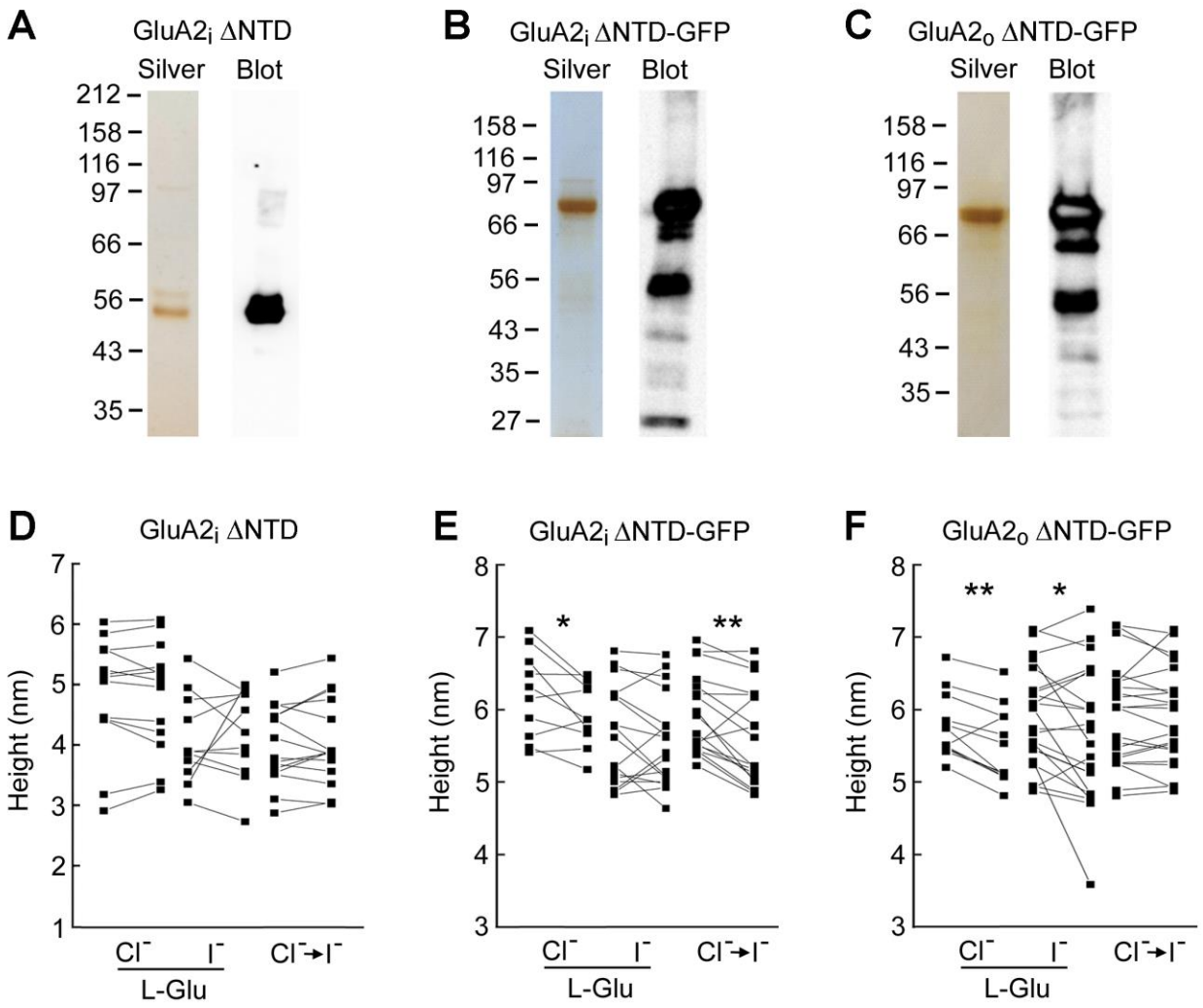
A
GluA2i ΔNTD
Silver
Blot
212
158
116
97
66
56
43
35
B
GluA2i ΔNTD-GFP
Silver
Blot
158
116
97
66
56
43
35
27
C
GluA2o ΔNTD-GFP
Silver
Blot
158
116
97
66
56
43
35
D
GluA2i ΔNTD
Height (nm)
Cl⁻
I⁻
Cl⁻→I⁻
L-Glu
E
GluA2i ΔNTD-GFP
*
**
Height (nm)
Cl⁻
I⁻
Cl⁻→I⁻
L-Glu
F
GluA2o ΔNTD-GFP
**
*
Height (nm)
Cl⁻
I⁻
Cl⁻→I⁻
L-Glu

Figure S7

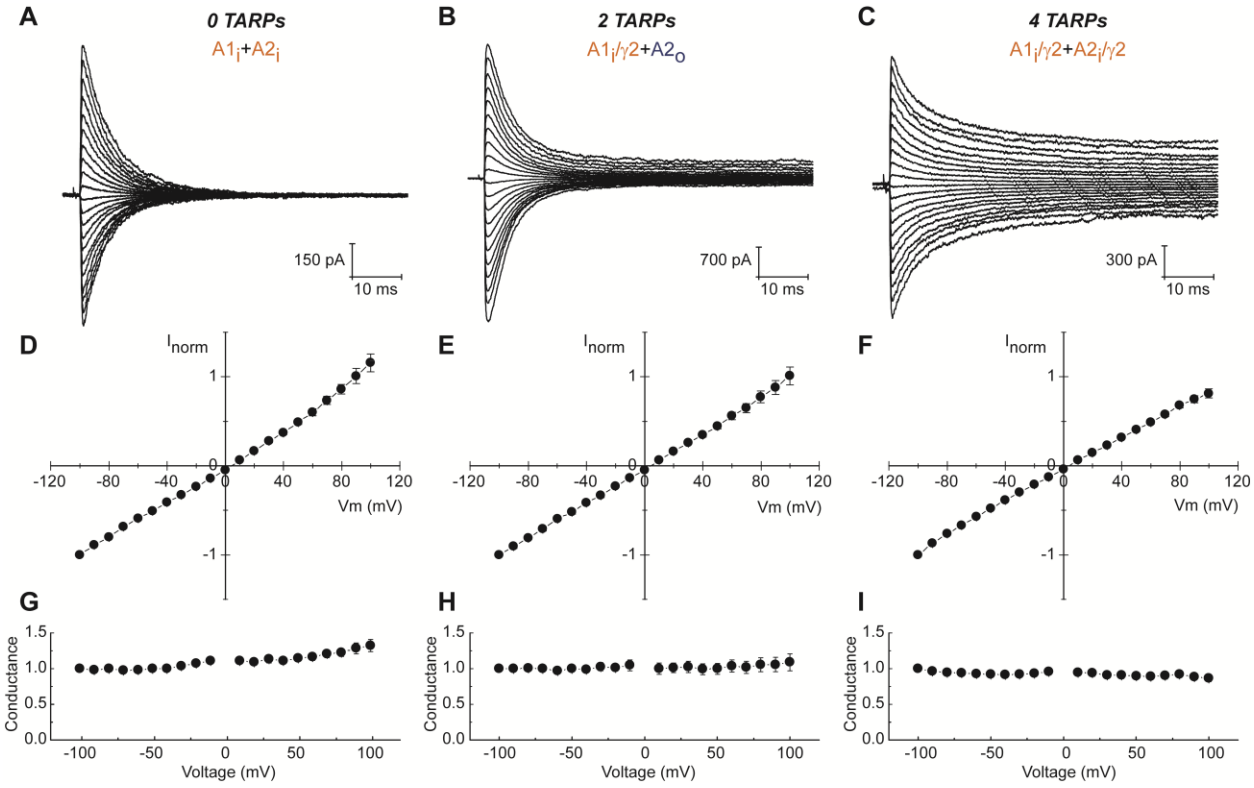
A
0 TARPs
A1i+A2i
150 pA
10 ms
B
2 TARPs
A1i/γ2+A2o
700 pA
10 ms
C
4 TARPs
A1i/γ2+A2i/γ2
300 pA
10 ms
D
E
F
Inorm
Vm (mV)
G
H
I
Conductance
Voltage (mV)

SUPPLEMENTAL FIGURES TITLES AND LEGENDS

Figure S1. Bromide ions in the GluA2-LBD dimer interface and sensitivity to cyclothiazide, Related to Figure 2. (A) Alignment of the $GluA2_o$ (magenta/blue) and "flip-like" $GluA2_o$-LBD N775S (cyan/orange) LBD dimers. Bromide ions at the dimer interface are shown as spheres ($GluA2_o$, grey; N775S, red). L-Glu is shown in green sticks representation. Nitrogen atoms are shown in blue and oxygen atoms in red. Left: side view; right: top view. Occupancy of bromide ions was refined to 0.4. **(B)** Anomalous difference electron density map (before introduction of bromide ions in the structure) from $GluA2_o$-LBD N775S, contoured at 7σ. Two bromide ions (1) were located in the vicinity of Pro515 at the dimer interface. **(C)** Anomalous difference electron density map from $GluA2_o$-LBD (chain A), contoured at 7σ. In addition to two bromide ions (1) located at the dimer interface, bromide ions lining the side chain of Arg506 in the glutamate binding site (2) and bromide ions involved in crystal packing (3) were observed in this structure. **(D)** Fo-Fc difference map (green; contoured at 3σ) from refining with water molecule instead of bromide ion in GluA2o-LBD N775S. A 2Fo-Fc electron density map (grey; contoured at 1σ) is shown for the bromide site and water molecules within 4 Å from the bromide site. **(E)** Fo-Fc difference map (green; contoured at 3σ) from refining with water molecule instead of bromide ion in GluA2o-LBD (chain A). A 2Fo-Fc electron density map (grey; contoured at 1σ) is shown for the bromide site and water molecules within 4 Å from the bromide site. **(F)** Top views of the $GluA2_o$-LBD N775S dimer (PDB: 3H6T; cyan/orange), showing two CTZ molecules (yellow sticks) bound in the dimer interface, aligned with bromide ions (brown spheres). **(G)** Response of $GluA2_i$ receptors to a sustained (250 ms) application of 10 mM L-Glu in different external halide ions, prior to (black) and during (blue) CTZ exposure. Responses in NaCl (patch 160516p4), NaBr (patch 160512p4), and NaI (patch 160510p4) were obtained from separate patch experiments. **(H)** Mean equilibrium current amplitude ($I_{equilibrium}$) of $GluA2_i$ receptors, as a percentage of the peak response (left axis, grey), in NaCl prior to CTZ application (Con.), or various halide ions in the presence of CTZ. The potentiation of the peak current response induced by CTZ in the same set of ionic conditions is also shown (right axis, blue). Data are mean ± SEM, from six (NaCl, NaI) or seven (NaBr) independent patch experiments.

Figure S2. Mutation of residue Leu504 disrupts anion modulation of AMPAR desensitization, Related to Figure 3. (A-B) Side (A) and zoom-in (B) views of the $GluA2_i$ LBD dimer interface highlighting the Ser775 and Leu504 residues in proximity to bromide ions (brown spheres) at the anion binding site. **(C-D)** Typical current responses of $GluA2_i$ L504C (C) and L504A (D) receptors to a 250 ms application of 10 mM L-Glu in external NaCl (black), NaBr (dark grey), and NaF (light grey). Inset: scaled responses in different external anions to compare decay kinetics. The uppermost trace (black) shows the junction current recorded after each experiment to monitor solution exchange. **(E-F)** Mean time constants of current decay (E) and mean equilibrium current amplitude as a percentage of the peak response (F) after a 250 ms L-Glu application for the experiments described in panels C and D, in the presence of different external anions. **(G)** Average height changes of $GluA2_i$, $GluA2_o$ and $GluA2_i$ L504A in response to L-Glu. Data are mean ± SEM for 10-14 receptors. **(H)** Average height changes of $GluA2_i$, $GluA2_o$ and $GluA2_i$ L504A in response to anion switches. Data are mean ± SEM for 10-15 receptors.

Figure S3. The GluA2$_i$ T765N/P766A mutations do not influence anion sensitivity unless S775N is present, Related to Figure 3. (A-B) Typical current responses of GluA2$_i$ T765N/P766A (A) and T765N/P766A/S775N (B) receptors to a 250 ms application of 10 mM L-Glu in external NaCl (black), NaBr (cyan), and NaI (blue). Inset: scaled responses to compare decay kinetics including a representative response in NaF (grey). The uppermost trace (black) shows the junction current recorded after each experiment to monitor solution exchange. **(C-D)** Representative voltage-clamp traces showing recovery from desensitization for GluA2$_i$ T765N/P766A (C) and T765N/P766A/S775N (D) receptors in external NaCl (black) and NaI (dark blue). Both ionic conditions were recorded from the same patch. **(E)** Mean time constants of current decay after a 250 ms L-Glu application (τ_{des}) for the experiments described in panels A and B, in the presence of different external anions. **(F)** Mean time constants of recovery from desensitization for GluA2$_i$ T765N/P766A and T765N/P766A/S775N receptors in the presence of different external anions.

Figure S4. **AFM imaging of bilayer-integrated AMPARs, Related to Figure 4**. **(A)** Isolation of HA-tagged GluA2$_i$, GluA2$_o$ and GluA2$_i$ S775N, by anti-HA immunoaffinity chromatography. Samples were analyzed by SDS-PAGE followed by either silver staining (left panels) or immunoblotting using an anti-HA antibody (right panels). **(B)** Schematic illustration of the engagement of the AFM tip with a single AMPAR. **(C)** AFM image (2 μm x 2 μm) of a protein-free lipid bilayer. Scale bar, 400 nm; color-height scale, 0-10 nm. **(D)** AFM image (2 μm x 2 μm) of bilayer-integrated GluA2$_i$ receptors. Arrows indicate receptor positions. Scale bar, 400 nm; colour-height scale, 0-10 nm. **(E)** Frequency distribution of heights of the GluA2$_i$ particles in bilayers. The curve indicates the fitted Gaussian functions. The peaks of the distribution (±SEM) are indicated. Based on our previous experience with AFM imaging of NMDA receptors (Suzuki et al., 2013), we assumed that particles in the taller population (peak 7.2 nm) represent assembled AMPARs. Particles in the shorter population (peak 4.7 nm) likely represent a mixture of unfolded or incompletely assembled receptors, together with receptors integrated into the bilayer cytoplasmic side-up. Only the assembled receptors were subjected to analysis. **(F)** Zoomed AFM image (200 nm x 200 nm) of a GluA2$_i$ receptor decorated by two anti-HA antibodies. Scale bar, 50 nm; color-height scale, 0-13 nm. The paired-globule appearance of the NTD layer is clearly visible in this zoomed image. The height of the antibody-decorated receptor falls within the taller of the two populations shown in (E). A schematic illustration of the decorated receptor is shown at the right of the AFM image.

Figure S5. Effect of L-Glu and anions on AMPAR height, Related to Figure 4. (A-L) Heights of individual GluA2 AMPARs before (left-hand point) and after (right-hand point) the indicated anion switch or addition/washout of L-Glu. The asterisks indicate statistical significance (*$p < 0.05$; **$p < 0.01$; ***$p < 0.001$; Student's paired, two-tailed t-test). Drug concentrations were: L-Glu, 10 mM; CNQX, 0.5 mM; CTZ, 0.1 mM.

Figure S6. **Effect of L-Glu and anions on the height of individual truncated AMPARs, Related to Figure 4. (A-C)** Isolation of HA-tagged GluA2$_i$ ΔNTD (A), GluA2$_i$ ΔNTD-GFP (B) and GluA2$_o$ ΔNTD-GFP (C) by anti-HA immunoaffinity chromatography. Samples were analyzed by SDS-PAGE followed by either silver staining (left panels) or immunoblotting using anti-HA antibody (right

panels). **(D-F)** Heights of individual GluA2$_i$ ΔNTD (D), GluA2$_i$ ΔNTD-GFP (E) and GluA2$_o$ ΔNTD-GFP (F) receptors before (left-hand point) and after (right-hand point) either addition of L-Glu or Cl^--to-I^- anion switch. Asterisks indicate statistical significance (*p < 0.05; **p < 0.01; Student's paired, two-tailed t-test).

Figure S7. GluA2(R)-containing heteromers are not blocked by polyamines, Related to Figure 8. (A-C) Example traces from GluA1$_i$+GluA2$_i$ (A, patch 190201p7), GluA1$_i$/γ2+GluA2$_o$ (B, patch 190204p4), and GluA1$_i$/γ2+GluA2$_i$/γ2 (C, patch 190215p5) exposed to 5 mM L-Glu (250 ms) at different membrane potentials (range, -100 to 100 mV, 10-mV increments) in the presence of 30 μM internal spermine (Spm). **(D-F)** Mean I–V plots, normalized to +100 mV in Spm, for the receptor complexes shown in A-C. **(G-H)** Mean G–V plots for the receptor complexes shown in A-C. Data are mean ± SEM.

Table S1. Gating behavior of GluA2 receptors in the presence of different external anions, Related to Figures 1, 3, and 6. Wildtype and mutant GluA2 flip (i) and flop (o) isoform receptors were expressed alone or with γ2.

	I	Br	Cl	F	Propionate
$GluA2_i$					
$\tau_{desensitization}$	1.6 ± 0.1 (7)	4.3 ± 0.2 (7)	7.3 ± 0.3 (15)	9.2 ± 0.4 (8)	10.4 ± 0.8 (7)
$I_{equilibrium}$ (%)	0.6 ± 0.08	0.6 ± 0.09	1.1 ± 0.1	2.1 ± 0.3	3.3 ± 0.3
I_{norm}	0.64 ± 0.07	0.93 ± 0.04	*1*	0.54 ± 0.05	0.23 ± 0.03
$\tau_{deactivation}$	0.5 ± 0.04 (5)	0.5 ± 0.04 (7)	0.5 ± 0.03 (12)	0.5 ± 0.04 (7)	-
$\tau_{recovery}$	62.5 ± 3.0 (6)	37.2 ± 5.4 (7)	24.1 ± 1.5 (13)	-	-
$GluA2_o$					
$\tau_{desensitization}$	0.8 ± 0.05 (6)	1.1 ± 0.08 (6)	1.3 ± 0.06 (12)	1.7 ± 0.14 (6)	1.3 ± 0.05 (6)
I_{norm}	0.60 ± 0.03	0.84 ± 0.04	*1*	0.54 ± 0.04	0.20 ± 0.03
$\tau_{recovery}$	50.8 ± 5.2 (7)	35.0 ± 3.0 (13)	21.3 ± 1.2 (32)		-
$GluA2_i$ S775N					
$\tau_{desensitization}$	3.6 ± 0.5 (6)	3.4 ± 0.2 (6)	5.2 ± 0.4 (12)	5.8 ± 0.4 (6)	5.6 ± 0.6 (6)
I_{norm}	1.06 ± 0.10	1.05 ± 0.06	*1*	0.46 ± 0.05	0.25 ± 0.02
$\tau_{recovery}$	40.9 ± 3.1 (5)	23.3 ± 1.9 (5)	15.1 ± 0.9 (9)	-	
$GluA2_i$ T765N/P766A					
$\tau_{desensitization}$	0.7 ± 0.05 (9)	2.2 ± 0.2 (13)	2.9 ± 0.2 (25)	4.1 ± 0.3 (8)	-
$\tau_{recovery}$	37.1 ± 2.8 (7)	23.2 ± 2.1 (11)	15.1 ± 0.7 (22)	-	-
$GluA2_i$ L504A					
$\tau_{desensitization}$	17.2 ± 1.1 (5)	20.1 ± 1.4 (5)	14.5 ± 0.7 (10)	5.7 ± 0.9 (5)	8.6 ± 0.8 (5)
I_{norm}	0.69 ± 0.08	0.86 ± 0.05	*1*	0.39 ± 0.05	0.24 ± 0.05
$\tau_{recovery}$	96.3 ± 13.1 (6)	32.9 ± 4.2 (6)	22.0 ± 2.8 (12)	-	-
$GluA2_i$ ΔNTD					
$\tau_{desensitization}$	2.6 ± 0.1 (5)	6.8 ± 0.4 (6)	15.1 ± 0.6 (6)	19.0 ± 1.5 (6)	-
$\tau_{recovery}$	43.3 ± 6.0 (5)	22.2 ± 1.4 (6)	12.7 ± 1.1 (10)	-	-
$GluA2_i$/γ2					
$\tau_{desensitization}$	-	13.4 ± 1.4 (8)	29.6 ± 2.5 (8)	39.7 ± 2.8 (8)	-
$I_{equilibrium}$ (%)	-	12.2 ± 1.5	22.6 ± 1.7	33.2 ± 1.7	-
$GluA2_o$/γ2					
$\tau_{desensitization}$	-	1.4 ± 0.1 (8)	1.7 ± 0.09 (8)	4.3 ± 0.4 (8)	-
$I_{equilibrium}$ (%)	-	2.2 ± 0.4	2.8 ± 0.4	6.1 ± 1.0	-
$GluA2_i$ S775N + γ2					
$\tau_{desensitization}$	-	4.6 ± 0.3 (8)	8.2 ± 0.7 (12)	14.7 ± 0.9 (9)	-
$I_{equilibrium}$ (%)	-	2.9 ± 0.5	5.9 ± 0.6	11.7 ± 1.4	-

GluA2 receptors were activated by long application (250 or 500 ms) or short (1 ms) applications of 10 mM L-Glu to measure desensitization and deactivation kinetics, respectively. In the presence of auxiliary subunits, current decay associated with desensitization was fit using bi-exponential functions to obtain the components τ_{fast} and τ_{slow}. Weighted time constants ($\tau_{desensitization}$) were calculated based on the relative area fit by the fast and slow components. Time constants are listed in ms and I_{norm} refers to peak current amplitudes relative to the same receptor recorded in chloride. The number of patch recordings for each condition (n) is indicated, and all values are mean ± SEM.

Table S2. Data collection and refinement statistics, Related to Figure 2.

	GluA2$_o$-LBD (NaBr)	**GluA2$_o$-LBD N775S (RbBr)**
Data collection		
Wavelength	0.91949	0.91976
Space group	*P*2	*C*2
Cell dimensions		
a, *b*, *c* (Å)	46.7, 47.7, 116.7	123.0, 47.5, 49.8
α, β, γ (deg.)	90, 93.8, 90	90, 110.2, 90
No. in asymmetric unit	2	1
Resolution (Å)	46.6-1.95 (2.06-1.95)[a]	46.8-1.75 (1.84-1.75)
No. unique reflections	37,848 (5,450)	27,430 (3,998)
R_{merge} (%)	8.9 (46.8)	7.4 (37.3)
$I/\sigma I$	7.8 (1.6)	7.5 (1.8)
Completeness (%)	100 (100)	100 (100)
Redundancy (merged/anomalous)	7.6 (7.6) / 3.9 (3.9)	5.0 (4.7) / 2.6 (2.6)
Refinement		
R_{work} / R_{free}[b] (%)	16.3/20.0	15.6/19.0
No. atoms		
Protein	4162	2092
Glutamate/bromide/other	20/6/12	10/1/23
Water	430	267
B-factors (Å^2)		
Protein	27.3/27.6	22.1
Glutamate/bromide/other	18.0/35.5/43.4	13.6/32.2/48.3
Water	31.5	28.7
R.m.s. deviations		
Bond lengths (Å)	0.005	0.0033
Bond angles (deg.)	0.74	0.71
Ramachandran plot		
Favored (%)	99.04	99.23
Outliers (%)	0	0

[a]Values in parantheses are for the highest resolution shell.
[b]5% of data were used for calculation of R_{free}.

Table S3. Summary of height change data, Related to Figure 4

Construct	Condition	Height reduction (nm)	SEM	Sample Size
GluA2i	Cl^- to Br^-	0.74	0.06	12
	Cl^- to I^-	0.87	0.11	13
	Br^- to Cl^-	-0.60	0.19	5
	I^- to Cl^-	-0.56	0.07	6
	L-Glu in Cl^-	0.69	0.11	11
	L-Glu in Cl^- washout	-0.58	0.16	6
	L-Glu in Br^-	0.25	0.05	14
	L-Glu in I^-	0.21	0.06	12
	L-Glu plus CNQX	-0.11	0.07	12
	L-Glu plus CTZ	-0.03	0.07	14
	Cl- to Br^- plus CTZ	0.45	0.19	6
	Cl- to I- plus CTZ	0.66	0.05	13
GluA2o	Cl^- to Br^-	0.03	0.06	14
	Cl^- to I^-	0.08	0.06	14
	L-Glu in Cl^-	0.61	0.07	10
	L-Glu in Br^-	0.70	0.14	10
	L-Glu in I^-	0.58	0.12	10
GluA2i S775N	Cl^- to I-	0.00	0.05	12
	L-Glu in Cl^-	0.56	0.10	10
	L-Glu in I^-	0.70	0.06	12
GluA2i L504A	Cl^- to Br^-	0.08	0.06	15
	Cl^- to I^-	0.04	0.13	10
	L-Glu in Cl^-	0.69	0.07	14
	L-Glu in Br^-	0.62	0.11	10
	L-Glu in I^-	0.74	0.09	10
GluA2i ΔATD	L-Glu in Cl^-	0.03	0.06	13
	L-Glu in I^-	0.13	0.10	11
	Cl^- to I^-	-0.05	0.08	15
GluA2i ΔATD-GFP	L-Glu in Cl^-	0.28	0.04	10
	L-Glu in I^-	0.06	0.10	17
	Cl^- to I^-	0.32	0.09	18
GluA2o ΔATD-GFP	L-Glu in Cl^-	0.27	0.07	12
	L-Glu in I^-	0.25	0.12	22
	Cl^- to I^-	0.02	0.06	22

Table S4. Combined and raw mobility data, Related to Figure 5.

Combined				
Construct	**Condition**	**CSD at 28 s (nm^2)**	**SEM**	**Sample Size**
$GluA2_i$	Control	5.58	0.92	5
	L-Glu (0.1 mM)	7.67	1.65	5
	L-Glu (1 mM)	7.13	0.95	3
	L-Glu (10 mM)	13.90	2.11	9
	L-Glu (10 mM) plus CNQX	5.33	0.82	4
$GluA2_o$	Control	15.53	2.54	7
	L-Glu (0.1 mM)	14.07	0.81	3
	L-Glu (1 mM)	12.04	0.83	3
	L-Glu (10 mM)	17.12	0.59	5
	L-Glu (10 mM) plus CNQX	9.50	1.95	3
$GluA2_i$ S775N	Control	14.00	1.70	9

Raw		
Construct	**Condition**	**CSD at 28 s (nm^2)**
$GluA2_i$	Control	8.12, 2.36, 5.81, 6.05, 5.57
	L-Glu (0.1 mM)	5.09, 2.46, 10.51, 10.06, 10.25
	L-Glu (1 mM)	8.50, 7.58, 5.30
	L-Glu (10 mM)	11.06, 15.71, 6.17, 18.42, 18.32, 4.69, 25.00, 12.63, 13.09
	L-Glu (10 mM) plus CNQX	5.53, 4.12, 4.12, 7.57
$GluA2_o$	Control	9.92, 9.28, 8.36, 20.53, 23.39, 23.24, 13.87
	L-Glu (0.1 mM)	13.64, 12.93, 15.64
	L-Glu (1 mM)	10.96, 11.47, 13.68
	L-Glu (10 mM)	16.41, 15.38, 17.17, 18.80, 17.83
	L-Glu (10 mM) plus CNQX	10.04, 5.89, 12.57
$GluA2_i$ S775N	Control	7.19, 16.08, 17.31, 20.41, 6.91, 15.74, 8.43, 18.31, 15.66

Table S5. Gating behavior of native AMPARs and GluA1/A2 heteromers in the presence of different external anions, Related to Figures 7 and 8.

	Br	Cl	F
Native Cells			
Purkinje Cell			
$\tau_{desensitization}$	3.9 ± 0.5 (5)	7.5 ± 0.4 (20)	10.6 ± 0.9 (6)
$I_{equilibrium}$ (%)	5.4 ± 2.0 (4)	8.3 ± 0.6 (21)	17.1 ± 2.8 (4)
$I_{equilibrium}$ in CTZ (%)	-	89.1 ± 2.5 (7)	-
$\tau_{deactivation}$	-	1.0 ± 0.1 (5)	-
Stellate Cell			
$\tau_{desensitization}$	2.0 ± 0.2 (8)	2.9 ± 0.1 (30)	5.0 ± 0.6 (5)
$I_{equilibrium}$ (%)	2.4 ± 0.5 (7)	1.4 ± 0.1 (29)	3.2 ± 0.5 (5)
$I_{equilibrium}$ in CTZ (%)	-	88.6 ± 3.2 (6)	-
$\tau_{deactivation}$	-	0.8 ± 0.04 (17)	-
A1/A2 Heteromers 0 TARPs			
A1i+A2i			
$\tau_{desensitization}$	3.2 ± 0.2 (6)	4.5 ± 0.3 (7)	7.9 ± 0.7 (6)
$I_{equilibrium}$ (%)	0.3 ± 0.1 (3)	0.8 ± 0.2 (7)	1.3 ± 0.3 (5)
A1o+A2o			
$\tau_{desensitization}$	1.7 ± 0.3 (4)	2.0 ± 0.1 (7)	2.4 ± 0.1 (6)
$I_{equilibrium}$ (%)	0.3 ± 0.2 (3)	0.0 (6)	0.3 ± 0.2 (4)
A1/A2 Heteromers 2 TARPs			
A1i/γ2+A2o			
$\tau_{desensitization}$	2.6 ±0 .4 (4)	3.4 ± 0.3 (8)	5.8 ± 0.8 (4)
$I_{equilibrium}$ (%)	0.0 (3)	1.5 ± 0.5 (8)	3.0 ± 2.5 (3)
A1o+A2i/γ2			
$\tau_{desensitization}$	3.6 ± 0.2 (2)	4.7 ± 0.2 (3)	7.8 ± 0.7 (2)
$I_{equilibrium}$ (%)	0.6 ± 0.1 (2)	1.1 ± 0.03 (3)	2.6 ± 0.05 (2)
A1o/γ2+A2i			
$\tau_{desensitization}$	4.8 ± 0.4 (6)	7.0 ± 0.4 (6)	12.0 ± 1.2 (6)
$I_{equilibrium}$ (%)	1.1 ± 0.3 (5)	1.5 ± 0.3 (6)	3.2 ± 0.5 (6)
A1i/γ2+A2i			
$\tau_{desensitization}$	-	8.2 ± 0.8 (10)	-
$I_{equilibrium}$ (%)	-	3.7 ± 0.9 (10)	-
A1i+A2i/γ2			
$\tau_{desensitization}$	-	6.9 ± 0.9 (7)	-
$I_{equilibrium}$ (%)	-	4.0 ± 0.9 (7)	-
A1/A2 Heteromers 4 TARPs			
A1i/γ2+A2i/γ2			
$\tau_{desensitization}$	6.6 ± 0.3 (5)	10.6 ± 0.3 (6)	19.4 ± 1.4 (6)
$I_{equilibrium}$ (%)	12.2 ± 1.2 (5)	18.5 ± 1.4 (6)	34.4 ± 1.3 (6)

A1i/γ2+A2o/γ2			
$\tau_{desensitization}$	2.7 ± 0.2 (5)	3.3 ± 0.3 (7)	7.9 ± 0.6 (6)
$I_{equilibrium}$ (%)	6.0 ± 0.6 (5)	7.1 ± 0.7 (7)	14.3 ± 1.3 (6)
A1o/γ2+A2i/γ2			
$\tau_{desensitization}$	6.3 ± 0.4 (8)	8.9 ± 0.5 (8)	16.8 ± 0.9 (8)
$I_{equilibrium}$ (%)	11.7 ± 1.1 (8)	14.3 ± 1.5 (8)	28.2 ± 2.0 (8)
A1o/γ2+A2o/γ2			
$\tau_{desensitization}$	2.2 ± 0.2 (6)	3.0 ± 0.2 (7)	4.8 ± 0.4 (7)
$I_{equilibrium}$ (%)	1.4 ± 0.6 (5)	3.5 ± 0.8 (7)	7.4 ± 1.0 (7)

For native receptors, outside-out and nucleated patches were excised from cerebellar Purkinje and stellate cells, respectively, and exposed to rapid application of 10 mM L-Glu (250 ms or 1 ms duration) to measure desensitization and deactivation kinetics. Recombinant GluA1/A2 heteromers were activated by application of 5 mM L-Glu (250 ms) to measure receptor desensitization. Current decay was fit using bi-exponential functions to obtain the components τ_{fast} and τ_{slow}. Weighted time constants ($\tau_{desensitization}$) were calculated based on the relative area fit by the fast and slow components. Time constants are listed in ms. $I_{equilibrium}$ refers to the steady-state current as a percentage of the peak response. The number of patch recordings for each condition (n) is indicated, and all values are mean ± SEM.